



TECHNICAL REPORT 0-6878-3
TXDOT PROJECT NUMBER 0-6878

Characterization of Aggregate Texture and Correlation with Surface Skid Resistance

Sareh Kouchaki
Hossein Roshani
Joaquin Bernardo Hernandez
Jorge A. Prozzi

August 2017; Published September 2018

<http://library.ctr.utexas.edu/ctr-publications/0-6878-3.pdf>



Technical Report Documentation Page

| | | | | |
|---|--|-----------------------------|--|--|
| 1. Report No. FHWA/TX-17/0-6878-3 | | 2. Government Accession No. | 3. Recipient's Catalog No. | |
| 4. Title and Subtitle Characterization of Aggregate Texture and Correlation with Surface Skid Resistance | | | 5. Report Date August 2017; Published September 2018 | |
| 7. Author(s) Sareh Kouchaki, Hossein Roshani, Joaquin Bernardo Hernandez and Jorge A. Prozzi | | | 6. Performing Organization Code | |
| 9. Performing Organization Name and Address Center for Transportation Research The University of Texas at Austin 3925 W. Braker Lane, 4 th Floor Austin, TX 78759 | | | 8. Performing Organization Report No. 0-6878-3 | |
| 12. Sponsoring Agency Name and Address Texas Department of Transportation Research and Technology Implementation Office P.O. Box 5080 Austin, TX 78763-5080 | | | 10. Work Unit No. (TRAIS) | |
| | | | 11. Contract or Grant No. 0-6878 | |
| 15. Supplementary Notes Project performed in cooperation with the Texas Department of Transportation and the Federal Highway Administration. | | | 13. Type of Report and Period Covered Technical Report September 2016 to August 2017 | |
| | | | 14. Sponsoring Agency Code | |
| 16. Abstract This report consists of two parts presenting the methodology developed by researchers to find the correlation between the texture and friction. The first part of this research study analyzed the micro-texture of aggregates by means of discrete Fourier transform (DFT) and power spectral density (PSD) function. Micro-texture of aggregates is a critical component of pavement texture as well as a major contributing factor in roadway safety, especially in low speed conditions. Comprehending the effects of specific wavelengths in micro-texture is essential in the design of pavements to achieve adequate skid resistance. Six aggregates from two different quarries were scanned using a developed line laser scanner (LLS) prototype. In the second part, this research study performed a series of statistical analyses of field-measured friction and texture data to find the texture-friction correlation. Three test sections with different pavement types were selected within the state of Texas. Data were collected at three locations in the right wheel path and three locations in the center of the lane for each test section. To measure the texture data, the researchers used the Circular Track Meter (CTM) and a line laser scanner (LLS). Friction measurements were obtained with the Dynamic Friction Tester (DFT) and Grip-Tester. The mean profile depth (MPD) was calculated by using the measured texture data. The relationship between the MPD values and the friction numbers obtained from the Grip-Tester and DFT was investigated at speeds of 50 and 70 km/h (31 and 44 mph). The repeatability and reliability of both the developed LLS prototype and the Grip-Tester were also evaluated, as well as the effect of test speed on friction measurement. The results indicated a strong positive correlation between the texture and friction data. Additionally, the developed LLS prototype was able to scan the pavement surface texture more accurately and precisely than the CTM. The Grip-Tester showed promising results compared to the DFT with regards to the friction measurement. | | | | |
| 17. Key Words Friction, Micro-texture, Line Laser Scanner, Discrete Fourier Transform, Power Spectral Density, Root Mean Square Roughness, Depth of Surface Smoothness. | | | 18. Distribution Statement No restrictions. This document is available to the public through the National Technical Information Service, Springfield, Virginia 22161; www.ntis.gov. | |
| 19. Security Classif. (of report) Unclassified | 20. Security Classif. (of this page) Unclassified | 21. No. of pages 68 | 22. Price | |



THE UNIVERSITY OF TEXAS AT AUSTIN
CENTER FOR TRANSPORTATION RESEARCH

Characterization of Aggregate Texture and Correlation with Surface Skid Resistance

Sareh Kouchaki
Hossein Roshani
Joaquin Bernardo Hernandez
Jorge A. Prozzi

| | |
|-----------------------|---|
| CTR Technical Report: | 0-6878-3 |
| Report Date: | August 2017; Published September 2018 |
| Project: | 0-6878-3 |
| Project Title: | Accelerating Innovation in Partnered Pavement Preservation |
| Sponsoring Agency: | Texas Department of Transportation |
| Performing Agency: | Center for Transportation Research at The University of Texas at Austin |

Project performed in cooperation with the Texas Department of Transportation and the Federal Highway Administration.

Center for Transportation Research
The University of Texas at Austin
3925 W. Braker
Austin, TX 78759

<http://ctr.utexas.edu/>

Disclaimers

Author's Disclaimer: The contents of this report reflect the views of the authors, who are responsible for the facts and the accuracy of the data presented herein. The contents do not necessarily reflect the official view or policies of the Federal Highway Administration or the Texas Department of Transportation (TxDOT). This report does not constitute a standard, specification, or regulation.

Patent Disclaimer: There was no invention or discovery conceived or first actually reduced to practice in the course of or under this contract, including any art, method, process, machine manufacture, design or composition of matter, or any new useful improvement thereof, or any variety of plant, which is or may be patentable under the patent laws of the United States of America or any foreign country.

Notice: The United States Government and the State of Texas do not endorse products or manufacturers. If trade or manufacturers' names appear herein, it is solely because they are considered essential to the object of this report.

Engineering Disclaimer

NOT INTENDED FOR CONSTRUCTION, BIDDING, OR PERMIT PURPOSES.

Research Supervisor: Dr. Jorge Prozzi

Acknowledgments

The authors express appreciation to the TxDOT Project Director, members of the Project Monitoring Committee and personnel from the Maintenance and Construction Divisions and the Austin, Bryan, Houston, San Antonio and Waco Districts for their valuable contribution during field testing.

Table of Contents

| | |
|---|----|
| Chapter 1. Introduction | 1 |
| 1.1. Pavement Skid Resistance | 1 |
| 1.2. Previous Studies on Texture Measurement | 2 |
| 1.3. Previous Studies on Friction-Texture Correlation | 4 |
| 1.4. Research Motivation and Scopes | 5 |
| Chapter 2. Development of the Scanner Prototype | 6 |
| 2.1. Introduction | 6 |
| 2.2. Line Laser Scanner Prototype | 6 |
| 2.3. The LLS Range of Measurement | 7 |
| 2.4. Block Measurement | 9 |
| 2.5. Scanning Interval | 11 |
| 2.6. LabVIEW Program | 11 |
| 2.6.1. Linear Laser Scanner (LLS) | 12 |
| 2.6.2. Translation Stage | 13 |
| 2.6.3. User Interface | 14 |
| 2.7. Repeatability of the LLS | 14 |
| 2.8. Tilt and Error Issues | 15 |
| 2.8.1. Background Color and Ambient Light | 16 |
| 2.8.2. Adjusting the Settings of LJ-Navigator 2 | 18 |
| 2.8.3. Test #1 | 18 |
| 2.8.4. Test #2 | 19 |
| 2.8.5. Test #3 | 21 |
| 2.8.6. Test #4 | 22 |
| 2.9. Combining Two Scanned Data | 23 |
| Chapter 3. Investigating the Aggregate Texture | 25 |
| 3.1. Introduction | 25 |
| 3.2. Material Preparation and Data Collection | 25 |
| 3.3. Numerical Methods | 27 |
| 3.3.1. Continuous and Discrete Signals | 27 |
| 3.3.2. Analog and Digital Signals | 28 |
| 3.3.3. Fourier Transform | 29 |
| 3.3.4. Discrete Fourier Transforms (DFT) | 31 |
| 3.3.5. Power Spectral Density (PSD) | 31 |

| | |
|---|----|
| 3.3.6. Root Mean Square Roughness and Depth of Surface Smoothness | 31 |
| 3.4. Result and Discussion | 32 |
| 3.4.1. Effect of Orientation | 32 |
| 3.4.2. Comparison of PSD Results..... | 33 |
| 3.4.3. Paired t-test | 34 |
| 3.4.4. Evaluation of Root Mean Square Roughness and Depth of Surface Smoothness | 35 |
| Chapter 4. Pavement Friction and Texture Correlation | 39 |
| 4.1. Introduction..... | 39 |
| 4.1.1. Measurement of Skid Resistance | 39 |
| 4.1.2. Measurement of Pavement Surface Texture | 43 |
| 4.2. Data Collection | 44 |
| 4.3. Results and Discussions | 46 |
| 4.3.1. Repeatability of Developed LLS Prototype | 46 |
| 4.3.2. Grip-Tester Results | 48 |
| 4.3.3. Relationship between the Texture and Friction | 50 |
| Chapter 5. Summary and Conclusions..... | 53 |
| 5.1. Part 1: Aggregate texture measurement..... | 53 |
| 5.2. Part 2: Correlation between Pavement Texture and Friction..... | 54 |
| References..... | 55 |

List of Figures

| | |
|--|----|
| Figure 2.1 a) The triangulation system of a laser, and b) the prototype including the frame and mounted laser | 7 |
| Figure 2.2 The LLS measurement range in X and Z-direction..... | 8 |
| Figure 2.3 Schematic of laser's scan area | 8 |
| Figure 2.4 Gage block placement in laser's scanning line | 10 |
| Figure 2.5 Laser's LabVIEW process flowchart..... | 13 |
| Figure 2.6 User interface of LLS program..... | 14 |
| Figure 2.7 Height profile of aggregate along y-direction (top), and corresponding standard deviation (bottom) | 15 |
| Figure 2.8 a) Unfiltered 3D scan of an aggregate, b) 3D scan of an aggregate after removing the errors at the edges, c) unfiltered 3D scan of a pavement surface, and d) 3D scan of a pavement surface after removing the errors at the edges..... | 16 |
| Figure 2.9 Spectral range of light (http://karnikakapoor.blogspot.com/2016/04/weirdness-colour-spectrum.html)..... | 17 |
| Figure 2.10 Using different background colors in measurement..... | 17 |
| Figure 2.11 a) Scanning an aggregate from left to right, b) X-Y view of the scanned aggregate, c) Scanning an aggregate from right to left, d) X-Y view of the scanned aggregate | 19 |
| Figure 2.12 Three interpolation modes in the LJ-Navigator 2..... | 20 |
| Figure 2.13 Comparing one X-direction profile of aggregate surface in dead zone and invalid modes | 22 |
| Figure 2.14 Comparing One Y-direction profile of aggregate surface in different Processing Time..... | 23 |
| Figure 2.15 Metal plate | 24 |
| Figure 2.16 Black-and-white view of the first scan, second scan, and the two datasets on top of each other..... | 24 |
| Figure 3.1 Aggregate particles | 25 |
| Figure 3.2 Microscopic view of texture surfaces of a) “Intensity” of aggregate A, b) “Intensity” of aggregate B, c) “Range” of aggregate A, and d) “Range” of aggregate B..... | 26 |
| Figure 3.3 Graphical example of (a) continuous- and (b) discrete-time signals (Hsu, 1995)..... | 28 |
| Figure 3.4 Example of analog and digital sampling (Alazartech) | 28 |
| Figure 3.5 Example of a periodic continuous signal (Hsu, 1995) | 29 |
| Figure 3.6 A non-periodic (top) and a periodic signal (bottom) (Hsu, 1995)..... | 30 |
| Figure 3.7 Scan of A1 in different angles a) 0°, b) 90°, c) 180°, and d) 270° | 33 |

| | |
|--|----|
| Figure 3.8 PSD of Aggregate A1 in different angles..... | 33 |
| Figure 3.9 Comparison of PSD values of all aggregates | 34 |
| Figure 3.10 The profile of aggregate A1 with the micro-scale filtered profiles | 36 |
| Figure 3.11 Root mean square roughness values in different sub-bands of wavelengths | 37 |
| Figure 3.12 Values of depth of surface smoothness in different sub-bands of wavelengths..... | 37 |
| Figure 4.1 a) The Grip-Tester attached to a vehicle, b) bottom view of the DFT, and c) the DFT connected to a water tank and DCC measuring the friction at the lane center path..... | 43 |
| Figure 4.2 a) The CTM powered by a battery measuring the texture at the right wheel path, and b) bottom view of the CTM..... | 44 |
| Figure 4.3 Graphical illustration of MPD calculation (26)..... | 44 |
| Figure 4.4 Illustration of test section and test location | 45 |
| Figure 4.5 a) Comparison of mean MPD values obtained from developed LLS prototype and CTM, b) Standard deviation of MPD values measured by developed LLS prototype and CTM at six test sections..... | 47 |
| Figure 4.6 Correlation between GN and DFT values at two speeds of 50 and 70 km/h | 49 |
| Figure 4.7 Plotted texture-friction data points including GN, DFT values, and MPD values | 52 |

List of Tables

| | |
|---|----|
| Table 2.1 Scanning Interval for Varying Gage Blocks..... | 9 |
| Table 2.2 Scanning Interval for a 5.0 mm Gage Block at Varying Locations..... | 10 |
| Table 2.3 Results of Test #2, Dead Zone and Interpolation Modes | 21 |
| Table 3.1 Aggregates Properties (BRSQC, 2016) | 26 |
| Table 3.2 Sub-Bands of Classification of Wavelengths | 35 |
| Table 3.3 Side-by-side Comparison of Texture Parameters in Different Wavelength Ranges..... | 38 |
| Table 4.1 Comparison of the LFC Measuring Devices (Descornet et al., 2006; Do and Roe, 2008; Andriejauskas et al., 2014)..... | 40 |

Chapter 1. Introduction

1.1. Pavement Skid Resistance

According to the Federal Highway Administration, in 2015 there were 18,695 fatalities in the United States resulting from roadway departure. Poor roadway conditions, especially due to wet weather, have been identified as a major contributing factor in roadway accidents. A vehicle's loss of traction on wet pavements, and the poor visibility resulting from splash-and-spray, stem from the pavement having inadequate cross-slope and surface texture. Skidding alone contributes to 15 to 35% of accidents that occur under wet conditions (Hoerner and Smith, 2002). Tire-pavement interaction therefore dictates the safety of motorists. The direct force developed in the tire-pavement interface is known as *skid resistance*, which is defined by the properties of the tire, the vehicle speed, and the pavement condition and texture. Pavement texture determines the resistance of the pavement surface to a vehicle sliding and skidding (Asi, 2007; Wang and Wang, 2013). The extent of skid resistance on any given pavement is dependent on the design of the surface texture, specifically its micro- and macro-texture, as this can affect the skid resistance, splash-and-spray, rolling resistance, and tire wear (Henry, 2000). Pavement design can therefore adjust surface pavement properties to provide the safety needed (Hoerner and Smith, 2002).

Pavement surface texture is influenced by many factors, such as aggregate type and size, mixture gradation, and texture orientation, among others. By definition, pavement texture is the result of the deviations of the surface layer from an actual planar surface (ASTM E867). The World Road Association has categorized pavement texture by its range of wavelengths (λ) and amplitudes (A). The standard specification organizations, such as the American Society for Testing Materials (ASTM E867), International Organization for Standardization (ISO 13473-1), and German Institute for Standardization (DIN on ISO 13473-1), have accepted and incorporated these definitions. The ISO 13473-1 refined the terms incorporating typical amplitudes (Sandberg, 1998) as follows:

- Micro-texture ($\lambda < 0.5$ mm, A = 1 to 500 μ m) (where λ is wavelength and A is amplitude)
- Macro-texture (0.5 mm $< \lambda < 50$ mm, A = 0.1 to 20 mm)
- Mega-texture (50 mm $< \lambda < 500$ mm, A = 0.1 to 50 mm)

Micro-texture refers to the small-scale texture of the aggregate surface, which controls the contact between the tire rubber and the pavement surface. Micro-texture is a function of aggregate particle mineralogy, petrology, and source (natural or manufactured), and is affected by environmental effects and the action of traffic (Kogbara et al., 2016). *Macro-texture* refers to the large-scale texture of the pavement surface due to the aggregate particle size and arrangement. In asphalt pavements, the mixture properties (aggregate shape, size, and gradation), which define the type of

mixture, control the macro-texture (Hall et al., 2009). Macro-texture provides drainage paths for water entrapped between the pavement surface and tire imprint. Therefore, it controls the thickness of the water film on the pavement surface, and therefore the potential of hydroplaning (Huang, 2003). *Mega-texture* has wavelengths in the same order of size as the tire/pavement interface. Examples of mega-texture include ruts, potholes, and major joints and cracks. These affect vibration in the tire walls but not the vehicle suspension, and therefore are strongly associated with noise and rolling resistance (Hall et al., 2009). Mega-texture is out of the scope of the current study.

Pavement friction is the result of a complex interplay between two principal frictional force components: adhesion and hysteresis. Although there are other components of pavement friction, such as tire rubber shear, they are insignificant when compared to the adhesion and hysteresis force components (Henry, 2000; Hall et al., 2009). Thus, friction can be viewed as the sum of adhesion and hysteresis. *Adhesion* is the friction that results from the small-scale bonding/interlocking of the vehicle tire rubber and the pavement surface. It is a function of the interface shear strength and contact area (Hall et al., 2009; Gunaratne et al., 2000). The *hysteresis* component of the frictional forces results from the energy loss created within the tire as it responds to the texture. Because the adhesion force is developed at the tire-pavement interface, it is most responsive to the micro-level asperities (micro-texture) of the aggregate particles. In contrast, the hysteresis force developed within the tire is most responsive to the macro-level asperities (macro-texture) formed in the pavement surface (Henry, 2000; Hall et al., 2009).

Macro and *micro-texture* of the pavement surface vary widely with the type and source of the aggregates. (Ahammed and Tighe, 2008). Accordingly, it is very important that the engineer takes careful consideration of the selection of aggregates. The aggregate selection should be based on (but not limited to) the shape, angularity, and texture of the aggregate particles. To provide enough stability and strength to the asphalt mixture, most specifications limit the amount of aggregate particles with rounded, smooth texture. Coarser aggregates increase the magnitude of the hysteresis component of the frictional force, since the tire material is deformed more on larger aggregates. Aggregates with rough micro-textures provide greater surface area between the tire and the pavement. In the case of wet pavements, a rougher micro-texture contributes to skid resistance by breaking the thin layer of water on the surface, promoting the contact between pavement and tire required to develop the interatomic attractive forces of the adhesion component (Serigos et al., 2014; Araujo et al., 2015; Wang et al., 2017; Hu et al., 2016).

1.2. Previous Studies on Texture Measurement

The Circular Track Meter (CTM) and the Sand Patch Test (SPT) are the two common measurement methods used by highway agencies to measure the macro-texture of the pavement. However, there is not a common method used by highway agencies to measure pavement micro-texture or the texture of aggregates. In recent research studies, laser scanners and imaging devices have been used to study pavement texture at both macro and micro levels (Chen et al., 2017; Zhang et al.,

2014; Wang et al., 2005; Slimane et al., 2008; Wang et al., 2017; Cafiso and Taormina, 2007; Abbas et al., 2007). Fourier transform analysis and power spectral density analysis are the common signal processing methods used in some of these research studies to evaluate surface texture. Fourier analysis provides an alternative representation of a waveform in which its frequency components can be observed and analyzed. According to the Fourier theory, all signals, whether real or arbitrary, can be represented as the sum of sinusoidal waves of various amplitudes and frequencies. The Fourier transform (FT) helps to find the amplitudes and frequencies of these constituent sinusoids. The surface roughness power spectrum, or power spectral density (PSD), can be derived using the FT from the measured height profile, which is the most important parameter of randomly rough surfaces.

Chen et al. used a 3D laser scanner and adopted a pressure-sensitive film to show that both micro- and macro-texture of asphalt pavement significantly depends on the proportion of coarse aggregates in the mixture (Chen et al., 2017; Zhang et al., 2014).

In 2005, Wang et al. implemented the Fourier morphological analysis method to quantify the surface texture of aggregates on a macro-scale, in order to then compare quantitative measurements with qualitative human-observation-based judgments. Researchers ranked and quantified ten different aggregates in terms of shape, angularity, and surface texture. The results showed that the orientation of the aggregate particles in the profile images did not significantly affect the surface texture factors of those particles having similar size; however, the texture factors might be quite different for the aggregates of different sieve size ranges (Wang et al., 2005).

Another study conducted by Slimane et al. in France sought to develop a new method to measure and characterize road surface micro-texture using image analysis. The power spectral density (PSD) of the high-frequency information obtained from surface cartography was studied. The PSD values were normalized and the aggregate surfaces were compared considering the PSD's standard deviation. The researchers then successfully used a combined method of geometric and frequential criteria to find a meaningful relationship between friction values and roughness descriptions (Slimane et al., 2008). Researchers at the RWTH Aachen University in Germany (Wang et al., 2017) used Fourier transformation to convert the surface texture information of the aggregates to a spatial frequency domain in order to investigate the wearing behavior of the aggregates. The two-dimensional power spectral density (2D-PSD) was calculated before and after a polishing test to evaluate the surface roughness and the texture changes. Comparing 2D-PSD values indicated that the polishing test affects surface texture only at very short wavelengths (below 62.8 micrometer).

Cafiso and Taormina used the average of PSD values for an aggregate sample to define a specific PSD characteristic of that sample. The results showed that this average value was reliable and operationally simple. The researchers believed that a graphic comparison between the PSD curves was insufficient to investigate the behavior of different types of aggregates during polishing tests due to a lack of quantitative evaluation. Hence, additional parameters—including the area under the PSD function that represents the mean-square roughness of the pavement; signal energy; slope

of the straight-line regression of the PSD function; and PSD index obtained by modal assurance criterion parameter—were introduced and used to appraise the position and form of PSD curves (Cafiso and Taormina, 2007).

In a comprehensive research study conducted by Abbas et al., the applications of different mathematical methods analyzing the texture surface of Portland cement concrete (PCC) was studied. Ten PCC field samples were scanned by X-ray Computed Tomography (CT) and analyzed by four methods: Hessian model, the Fast Fourier Transform (FFT), the wavelet analysis, and the PSD. The analyzed data were compared to the calculated mean profile depth (MPD). According to the findings, contrary to the wavelet energy, the FFT index could be used to distinguish between the samples surfaces based on smoothness and roughness. It was also capable of detecting the tines in pavement surface texture in terms of spacing and orientation. Results also showed that applying the PSD method for texture analysis allowed for proper identification of the anomalies that existed in the surface texture. Comparing the mathematical analyzed results to the MPD results, a high correlation between MPD and Hessian models and PSD indices was found (Abbas et al., 2007).

1.3. Previous Studies on Friction-Texture Correlation

Understanding the texture-friction relationship is valuable for transportation agencies and engineers to provide proper pavement maintenance and better design of asphalt mixtures. This would help the highway agencies to better select the aggregates and design the pavement texture, especially when higher skid resistance is needed. It can also decrease the costs of maintenance and most importantly, the rate of accidents.

In 2015, Torbruegge and Wies in Germany studied the correlation between wet skid resistance and pavement texture. Their findings showed no correlation between the mean texture depth (MTD) as a surface texture characteristic and skid resistance as measured by British Pendulum. Similar results were obtained by Gunaratne et al. (2000), who found no significant correlation between friction and MTD. However, Gunaratne et al. observed a strong correlation between friction and the texture frequency characteristics, such as the power spectral density (PSD) calculated by fast Fourier transform (FFT).

Kane et al. (2013) studied the pavement texture-friction relationship using the Hilbert–Huang transform as a signal processing technique to decompose the pavement texture, in order to define micro-texture parameters that can be correlated to the friction. Texture and friction data of the pavement were measured by the Circular Track Meter (CTM) and the Dynamic Friction Tester (DFT) respectively. The texture profile was decomposed into a series of basic functions called intrinsic mode functions (IMFs). Then, two base intrinsic mode functions (BIMFs) were developed. The results indicated a good correlation between some of those BIMFs parameters (including sharpness and density) and pavement friction (Kane et al., 2013).

The precise nature of the relationship between friction and texture remains unknown, although several attempts to reveal it have been made using methods such as Fourier, wavelet, and fractal analysis (Huang and Pan, 2006; Rado and Kane, 2014; Kane et al., 2013). These models' degree of complexity, and the difficulty in finding the coefficients relating to the calculations, results in complications for highway agencies.

1.4. Research Motivation and Scopes

Several studies have been conducted regarding pavement skid resistance and the role of pavement texture; however, the effects of pavement texture on friction is not fully understood. The Texas Department of Transportation (TxDOT) has developed a classification of aggregates based on their frictional and durability properties. Despite the importance of the aggregate texture in skid resistance, there is currently no texture measurement in TxDOT's aggregate classification to distinguish aggregates in terms of their texture. Aggregate texture corresponds to pavement micro-texture wavelengths.

This study was conducted in two parts. The purpose of the first part was to determine the dominant wavelengths in the micro-texture of aggregates that significantly contribute to the pavement surface friction. For this purpose, an accurate texture measurement device, herein referred to as the Line Laser Scanner (LLS), was developed. Then, the surface texture of various aggregates was analyzed using numerical methods such as discrete Fourier transform and power spectral density. By means of statistical analysis on PSD results, the most effective components of micro-texture were selected and were compared to surface friction parameters such as root mean square roughness (R_q) and depth of surface smoothness (R_p).

The focus of the second part was to find the correlation between field-measured texture data and friction. Regarding this, the LLS and the Circular Track Meter (CTM) were used to measure the pavement texture. The performance of the developed LLS prototype was evaluated by comparing its results with those of the CTM. To measure the friction of pavements, the Grip-Tester and the Dynamic Friction Tester (DFT) were used. Statistical analysis was employed to establish correlations between texture and friction.

Chapter 2. Development of the Scanner Prototype

2.1. Introduction

The main characteristic controlling the skid resistance of roadways is the surface texture, which is given by the sum of the macro and micro-textures. The Sand Patch Test (SPT) and the CTM are two common static methods used to measure the macro-texture of the pavement surface, but which cannot properly capture the texture at the micro level. There is not any common test or equipment in pavement industry capable of measuring the micro-texture directly. Therefore, a new method for the quantification of both micro- and macro-textures is required.

Developments in profiling technologies have facilitated the measurement of surface texture. Nowadays, a handful contact and non-contact types of profiling techniques are available (Poon and Bhushan, 1995; Vorburger and Raja, 1990). The superiority of non-contact type profilers is that no surface scratch is caused by the device during profiling (Sherrington and Smith, 1988). This chapter documents the development process of a three-dimensional non-contact profiler, which can be used to measure both micro-and macro-texture.

2.2. Line Laser Scanner Prototype

A line laser scanner (LLS) was utilized in this research study. This device is a two-dimensional (2D) non-contact laser sensor that projects blue light with a wavelength of 405 nm in a horizontal line. Generally, the line laser scanners available in the market work based on two different light colors: blue and red. The superiority of blue light over red light is its smaller wavelength, which results in less error and higher precision. The violet light is emitted from a source in the LLS and the reflection of the light from a given surface is then captured by a detector. If the angles between the projected light and the reflection are known then, by using triangulation, the height profile of the surface relative to the system's reference line can be calculated. Small changes in height due to the texture irregularities can also be captured using this scanner system. Figure 2.1(a) illustrates this triangulation system.

In this research study, a prototype (Figure 2.1(b)) was developed to enable the LLS to capture three-dimensional data. For this purpose, the LLS was mounted on a linear translation stage to travel over the surface and scan it. The developed LLS prototype is capable of collecting a maximum of 800 points in the transverse direction (X-direction) and a maximum of 15,000 points in the longitudinal direction (Y-direction). At each point, the LLS captures the relative height of that point, in millimeters (Z-direction). Combining the discrete height values captured in Y or X-direction provides height profiles. Therefore, the LLS is able to capture maximum 800 or 15000 parallel height profiles in Y or X-direction, respectively. While 800 points along the X-direction are captured at once and independent of time, the measurement along Y-direction depends on the speed of the scan and the frequency of the measurements. Both the linear translation stage and the

laser are connected to a computer, and the scanned data are collected there in an Excel file. Each row of the Excel file contains the scanned data in X-direction and each column contains the scanned data in Y-direction.

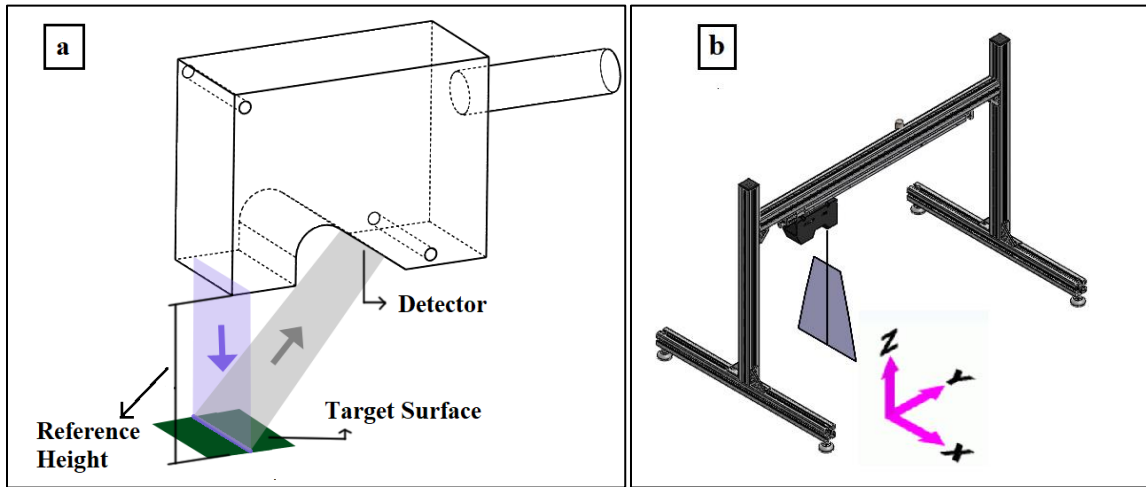


Figure 2.1 a) The triangulation system of a laser, and b) the prototype including the frame and mounted laser

During the use of the developed LLS prototype, researchers were faced with many issues regarding the measurement taking. The following explain the approaches employed to overcome those issues.

2.3. The LLS Range of Measurement

According to the laser specifications and manufacturer's instruction, the reference distance in Z-direction, which is the vertical distance between the laser and the object (Figure 2.2), is 80 mm. To achieve an acceptable measurement, the target should be close to the reference distance and within the measurement range of ± 23 mm in Z-direction. On the other hand, the measurement range in X-direction depends on the vertical distance of the target from the laser so that the closer distance to the laser, the narrower the measurement range in X-direction, as depicted in Figure 2.2. The measurement range in X-direction is 25 mm at near side, 32 mm at reference distance, and 39 mm at far side.

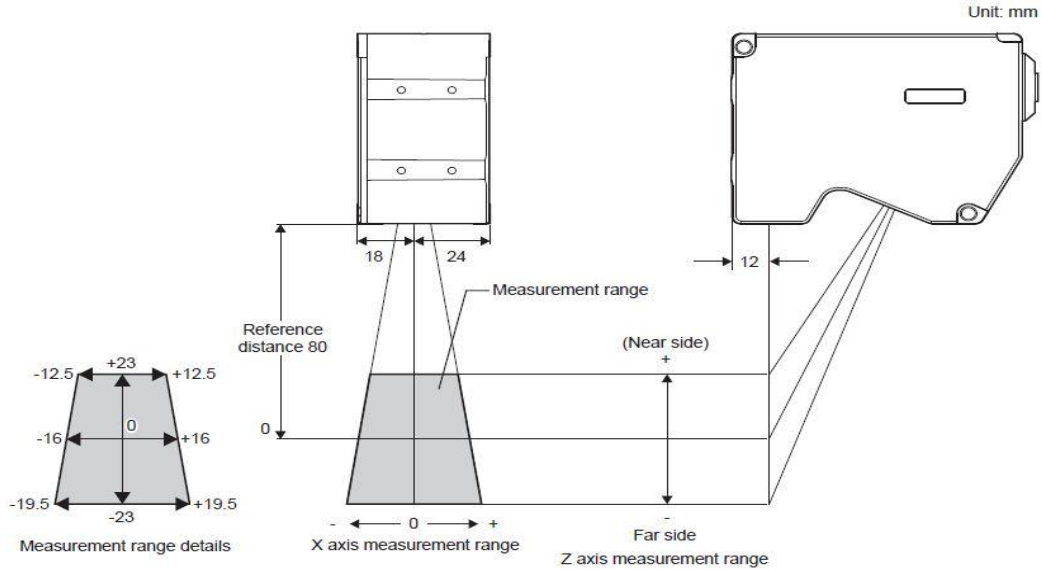


Figure 2.2 The LLS measurement range in X and Z-direction

After scanning, the points with extremely low values of -99.9999 mm, called negative dropouts, were recognized at the two sides of the laser line along with X-direction. Experiments to understand the negative dropouts at the edges of a profile were performed and it was found that the number of dropouts of the laser changed with height (Z-direction). The experiment led to the understanding of the quantity of dropouts observed as a result of different heights. As provided in Figure 2.3, when the laser head was fixed at a height of 60 mm from the surface being measured, the number of dropouts increases. Therefore, the X-direction had approximately 220 negative dropouts. When the laser head was fixed at its reference height of 80 mm, the number of dropouts were at approximately 95-100 points. Lastly, the laser head was fixed at 100 mm and it was found that there were no dropouts and the scan line was at its full 800 points in the X-direction.

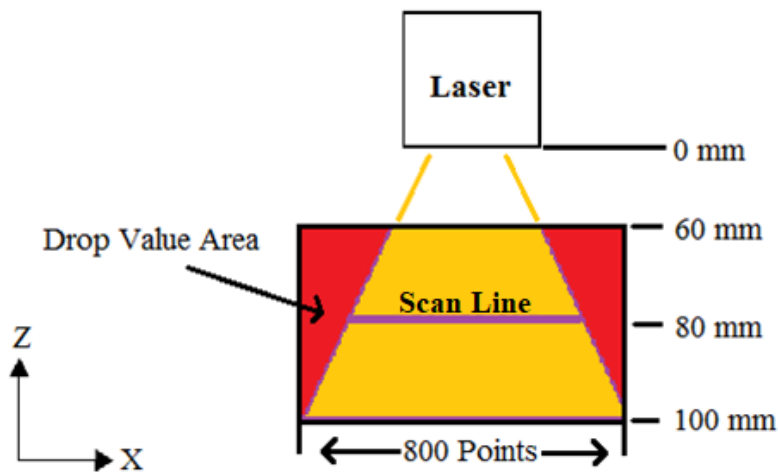


Figure 2.3 Schematic of laser's scan area

The results showed that an algorithm within the laser controller adds dropouts to the profiles based on the height. The closer the laser head is to the surface, the more dropouts there are and the less of the scan line. The opposite is true for when the laser is at approximately 100 mm: it has no dropouts and the full scan area can be used. This is done to keep the distance between two consecutive pints in the X-direction constant, i.e., 50 microns.

2.4. Block Measurement

As a result of the internal data processing done within the controller unit described above, the scanning interval in X-direction (ΔX) is fixed and equal to 50 microns. This following experiment was performed to understand how the differences in the height of the laser, the location of the object, and the object's width affected the profile data interval. Gage blocks with precisely manufactured dimensions were used as an object for this experiment. The gage blocks are certified by Fowler specifications with calibration traceable to the National Institute of Standards and Technology (NIST). Different sizes of gage blocks were used to understand how the object's width played a role in the measurement. The frame of the prototype is composed of two vertical supports that allow for the height of the laser to be adjusted. The variables in this experiment are as follows:

- Gage blocks width (mm): 5, 7.5, 10
- Height of the LLS (mm): 110, 100, 94, 80, 75, 70, 60

This experiment was performed in two parts. In the first, the focus was to see how the ΔX changed with varying gage block width. The placement of the gage blocks was in the middle of the laser's scanning line. Table 2.1 contains the ΔX for the respective gage block (5.0, 7.5 and 10.0 mm) and the reference height of the laser from the laser to the surface of the table. A single reading was taken for each experiment. To calculate the profile data interval in Excel the following Equation was used:

$$\Delta X = \frac{\text{Size of gage block (mm)}}{\text{Number of points in the measurement that make up the gage block}} \quad \text{Equation 2.1}$$

Table 2.1 Scanning Interval for Varying Gage Blocks

| Height | ΔX for 10mm | ΔX for 7.5mm | ΔX for 5mm |
|--------|---------------------|----------------------|--------------------|
| 110 mm | 0.0513 | 0.0500 | 0.0510 |
| 100 mm | 0.0508 | 0.0500 | 0.0500 |
| 94 mm | 0.0505 | 0.0497 | 0.0495 |
| 80 mm | 0.0526 | 0.0503 | 0.0500 |
| 75 mm | 0.0515 | 0.0500 | 0.0500 |
| 70 mm | 0.0518 | 0.0500 | 0.0510 |
| 60 mm | 0.0503 | | |

For the second part, the focus was to see how placing an object in different parts of the laser's scanning line would affect the profile data interval. Furthermore, the height of the laser and the surface were also investigated. A single gage block with the width of 5.0 mm was used throughout this experiment. The measurements consisted of three locations of the gage block for each height: right, center and left of the laser line. Figure 2.4 shows the placement of the 5-mm block at the center and the left of the laser line. The center location was measured with a ruler by taking the length of the scanning line and measuring the middle. The left and right locations depended on the height of the laser.

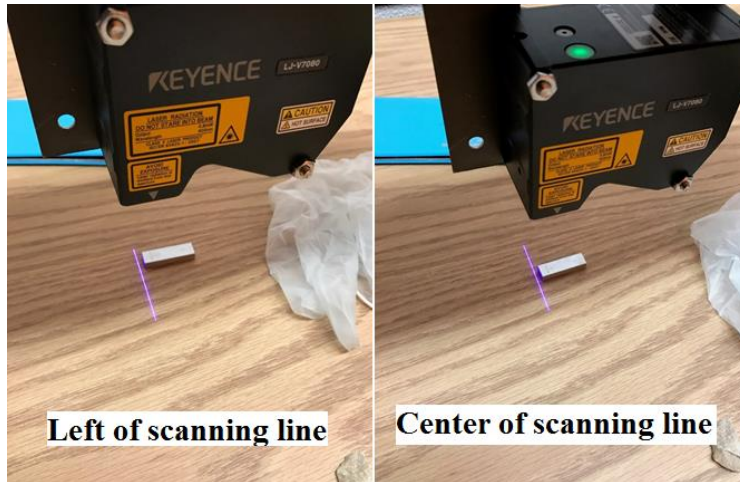


Figure 2.4 Gage block placement in laser's scanning line

Three different heights were tested: 100, 80, and 60 mm from the laser to the surface of the table, with three different scans per each location representing the left, center, and right. As seen in Table 2.2, a negative offset represents the right side and a positive offset represents the left side. Each location was scanned once.

Table 2.2 Scanning Interval for a 5.0 mm Gage Block at Varying Locations

| Height (mm) | Offset from center (mm) | ΔX Right | ΔX Center | ΔX Left |
|-------------|-------------------------|------------------|-------------------|-----------------|
| 100 | -10 | 0.0515 | | |
| 100 | 0 | | 0.0506 | |
| 100 | 10 | | | 0.0512 |
| 80 | -8 | 0.0521 | | |
| 80 | 0 | | 0.0503 | |
| 80 | 8 | | | 0.0515 |
| 60 | -5 | 0.0518 | | |
| 60 | 0 | | 0.0500 | |
| 60 | 5 | | | 0.0506 |

As a result of this experiment, it was found that when the object is placed in the middle of the scanning line and the object is thin enough for the scanning line to reflect from the edges of the object, the readings are found to be close to the profile data interval of 50 μm mentioned in the laser specification. The profile data interval then varies as the object gets further away from the center of the scanning line. This is mainly due to the edge furthest away from the center not being able to reflect back to the laser, hence increasing the uncertainty and reducing the accuracy. Accordingly, the reference distance of the laser from the background was kept at 80 mm and the objects were placed in the center of the laser line during the scans.

2.5. Scanning Interval

Micro-texture refers to the surface features with wavelength less than 0.5 mm and macro-texture refers to the features with wavelength between 0.5 and 50 mm. The focus of this study was on three ranges of wavelength including 1) the second decade of micro ($0.005 \text{ mm} < \lambda < 0.05 \text{ mm}$), 2) the first decade of micro ($0.05 \text{ mm} < \lambda < 0.5 \text{ mm}$), and 3) the first decade of macro ($0.5 \text{ mm} < \lambda < 5 \text{ mm}$). In order to capture the data in the second decade of micro-texture, based on Shannon theorem (Nyquist theorem) the interval between scanning points must be equal to half of the smallest wavelength of interest. Hence, in this case, the scanning interval is equal to 2.5 microns. Since the scanning interval in X-direction (ΔX) is 50 microns, scanning in X-direction cannot capture the second decade of micro-texture. To study the second decade of micro texture, the researchers used the scanning data in Y-direction. According to the Equation 2.2, scanning interval is related to both speed and the frequency of scanning so that different scanning intervals can be obtained by adjusting these two parameters in the LLS. For instance, by setting the frequency at 1 kHz and the moving speed at 2.5 mm/s, the scanning interval would be 2.5 microns.

$$\Delta y = v * \frac{1}{f} \quad \text{Equation 2.2}$$

where

Δy : scanning interval in Y direction

v : moving speed, mm/s

f : scanning frequency, Hz

2.6. LabVIEW Program

To operate the LLS and the linear translation stage, two corresponding computer codes were used simultaneously: LJ-Navigator 2 and Thorlabs APT User Interface, respectively. When performing a scan, the two computer codes worked independently of one another. Therefore, the APT User Interface had to start moving the LLS and then the operator had to switch quickly to the LJ-Navigator 2 to start collecting measurements from the LLS. This resulted in missing some data at the beginning of the scan and facing different start- and end-scan locations at different measurement runs.

In order to have reliable measurements, the two codes had to be merged into a single program that could start moving the laser while simultaneously collecting measurements with the LLS. This allowed the scans to be repeatable with the same start points, fixing the problems generated by having to use two independent pieces of software.

With the use of LabVIEW and instrument drivers, a program was developed. The development led to a program that operates a single laser head while also moving the translation stage. The program gives the user full control of the translation stage, similarly to the APT User Interface, allowing for conditions to be set, such as: starting position, speed, acceleration, and end position. The discussion of each separate component of the program is explained in the next paragraphs.

2.6.1. Linear Laser Scanner (LLS)

The laser program is the main focus of the code. The logic of it is composed of the following seven components listed below and can be visualized in the flowchart in Figure 2.5.

1. Communication Interface: Before running the program, the communication needs to be configured. A USB cable is used to transfer data from the laser's controller to the PC, and an Ethernet cable with sampling at rates faster than 2.0 kHz is highly recommended. The type of connection is selected in this step.
2. Start VI (Virtual Instruments): after configuring the communication with the laser, the LabVIEW VI program can be started at this time.
3. Idle: The VI runs and awaits the communication between the computer and the laser's controller. At this step, the translation stage can be configured to operate with user defined conditions. Such conditions include: speed, acceleration, start position, and end position.
4. Data Communication: A Start/Stop button was programmed to initiate and terminate the communication between the computer and the controller. Data are not stored at this point.
5. Start Monitoring: A Start/Stop button was programmed to initiate and terminate the reading and storing of the profiles by the lasers. Note: The Start/Stop button operates the motion of the translation stage as well.
6. Read Profiles: Profiles are read and saved to the computer, a height graph starts displaying batches of profiles. Indicator boxes display the profiles read and the buffer usage. The buffer usage is a percentage, which represents the temporary storage of the profiles. Warning: if the buffer usage reaches 100, the storage is saturated with profiles and data are lost.
7. Stop Reading Profiles: A Start/Stop button can be used to commence or end the profile readings. The number of readings is only restricted by the amount of capacity in the data storage and by the length of the translation stage which is 150 mm.

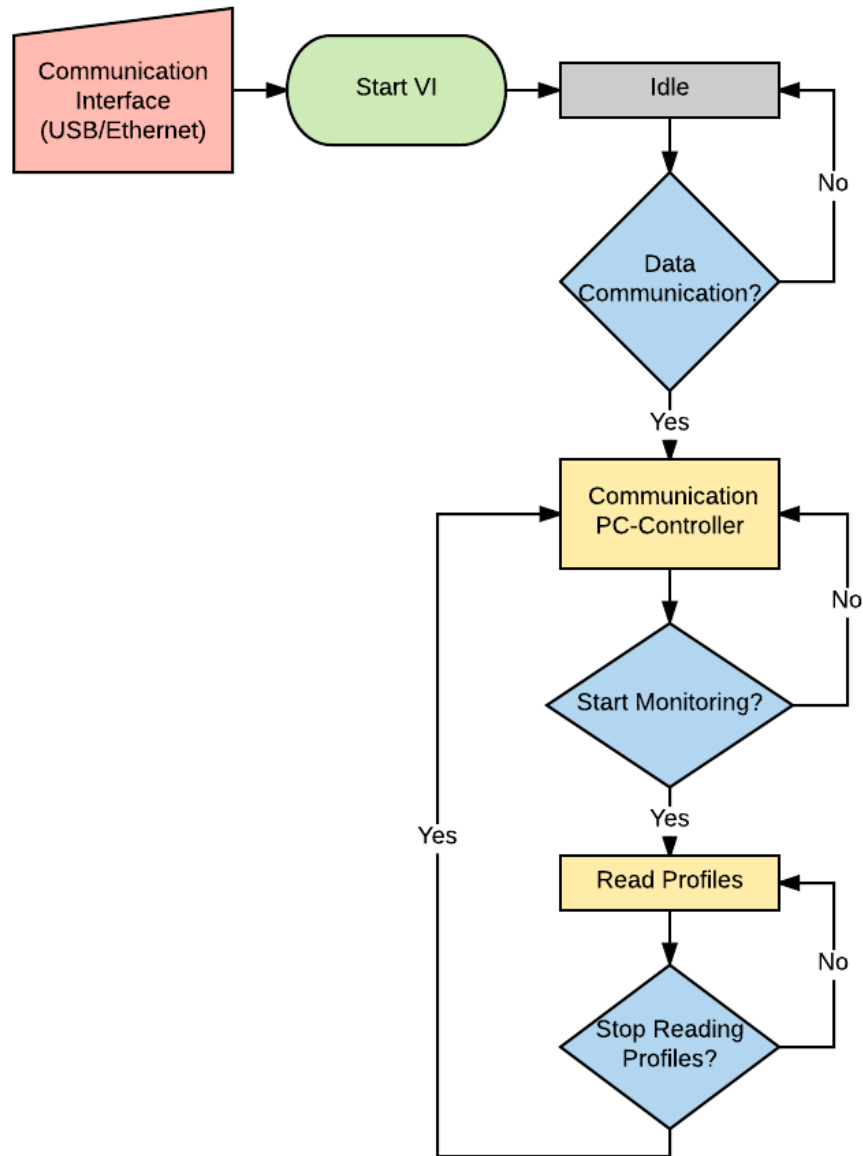


Figure 2.5 Laser's LabVIEW process flowchart

2.6.2. Translation Stage

As mentioned, the LLS is the main focus of the program, while the translation stage is embedded within the main program and operates as a SubVI. This means that the translation stage can be operated independently of the LLS but is connected to the main program and signaled to move by step 5, as mentioned above. The configuration screen allows the user to set conditions before the program starts running. This can be defined in step 3, before the LLS starts communicating with the controller. Furthermore, after the configuration of settings, the user clicks on the “Read Profiles Start/Stop” and the translation stage SubVI receives the signal to start operating if it was given a set position to move.

2.6.3. User Interface

Figure 2.6 shows the user interface that contains seven components including the graph of the real-time grayscale image and an easy-to-use control for the translation stage. When ready to use the program, the user follows the list above to start acquiring data from the LLS. When the program starts, the graphs labeled “Height Image” displays a corresponding height image in a grayscale. While the LLS is in motion and scanning, the graph provides the user an acknowledgment that the program is running. If aggregates are scanned, a real-time image of the aggregates can be seen.

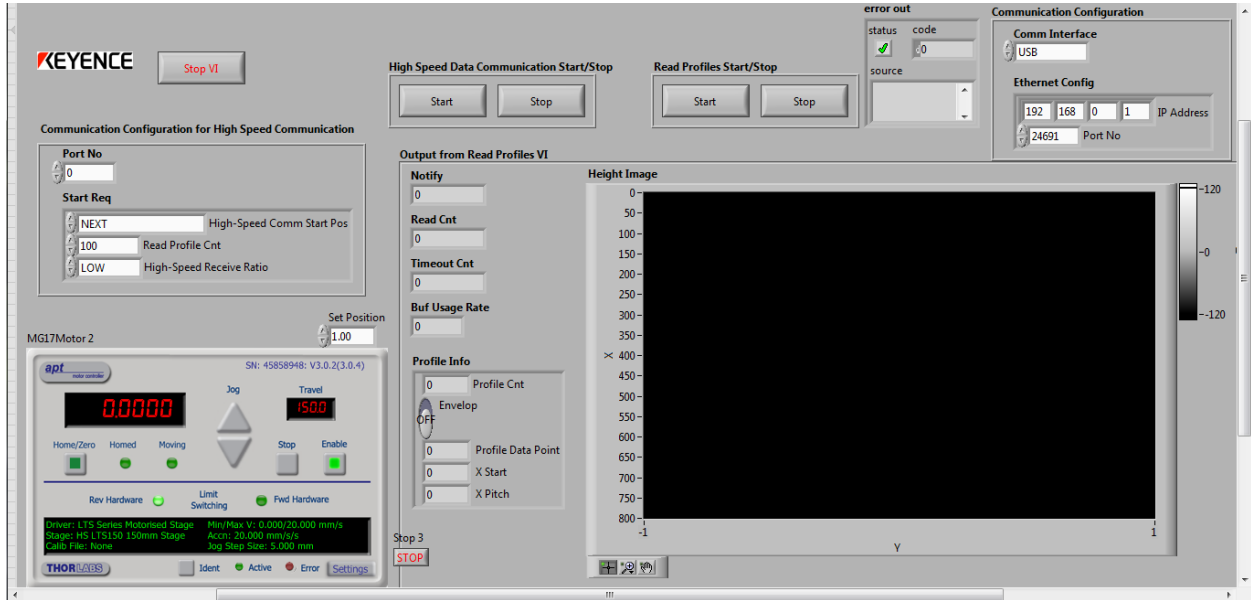


Figure 2.6 User interface of LLS program

2.7. Repeatability of the LLS

The LLS specification provides the repeatability in X and Z-direction of 10 and 0.5 microns, respectively. The repeatability of the developed prototype in Y-direction is required to ensure the accuracy of the measurements. The surface of an aggregate particle was scanned five times in Y-direction to check the repeatability of the LLS and the reliability of captured data. The repetitive scanning was performed under the same conditions without moving the developed LLS prototype or the aggregate. The height profiles located in the middle of the scanned data was selected from the five scans. As an example, a profile captured from the particle surface in Y-direction is depicted in Figure 2.7. The horizontal axis in these figures represents the number of points that were scanned in Y-direction with scanning interval of 2.5 microns and the vertical axis shows the height values. To study the repeatability, the standard deviation of five profiles was calculated and plotted along Y-direction below the height profile in Figure 2.7. According to this figure, at all scanned points the standard deviation of five height values was greater than 5 microns. In addition, higher standard deviations were observed within the areas in which the longitudinal profile was steep. Therefore, it can be concluded that the laser measurement was not reliable in the second decade of the micro-texture. Hence, the research team decided to study the data within the range of the first decade of

micro- and macro-texture, which is above 50 microns. Accordingly, the scan speed and frequency were adjusted to obtain the scanning interval of 25 microns.

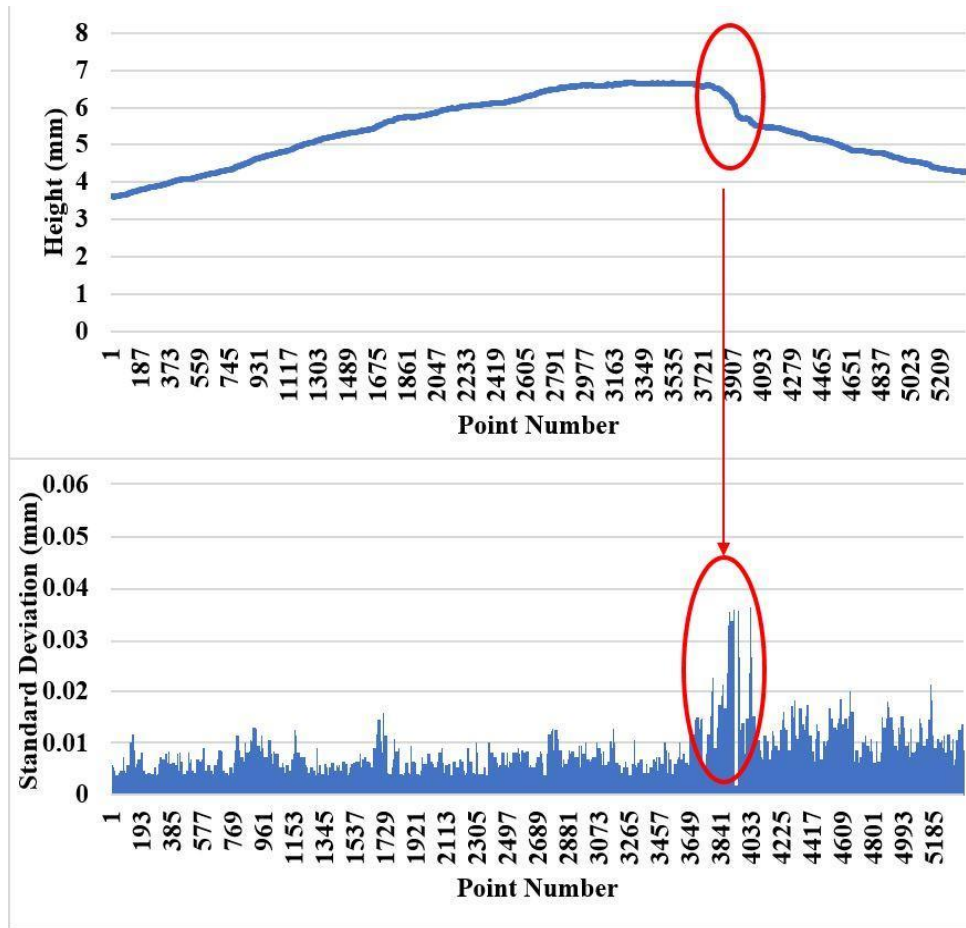


Figure 2.7 Height profile of aggregate along y-direction (top), and corresponding standard deviation (bottom)

2.8. Tilt and Error Issues

It is ideal to have a leveled surface for the measurement in order to minimize measurement errors. However, in some cases, the presence of laser line tilt in X-direction is inevitable due to the slope in the existing surface or the laser head, hence, tilt correction is required. This correction can be done automatically through the LJ-Navigator 2. In addition, before the data processing, the slope line of the scanned surface in Y-direction must be leveled to diminish the errors in the future calculations.

Dropouts, which are the points with either very high or low depth value, are recognized as errors. These errors are caused when the laser is not able to detect the light reflection. These errors are usually located at the edges of an object or at the holes. Figures 2.8(a) and 2.8(c) provide scans of an aggregate and a pavement surface, respectively. As shown in Figures 2.8(a) and 2.8(c), the negative dropouts can be found at the two sides of the laser line along with X-direction. To remove

these errors from analysis, fifty columns in each edge were trimmed out from the stored data. Thus, the final Excel data (as shown in Figure 2.8(b) and 2.8(d)) consisted of 700 points in each row. Points with high depth values mainly occurred during the scan of pavement surfaces. Using linear interpolation, those spikes were smoothed. As shown in Figure 2.8(b), dropouts exist around the aggregate edges. According to the ASTM E 1845, the number of dropouts of a profile should not exceed 10 percent of that profile (ASTM E 1845, 2009). Several factors such as background color, glossiness, ambient light, scanner settings, etc. might affect the quality of scanned data. Accordingly, researchers have studied the influence of these factors on the scanned data.

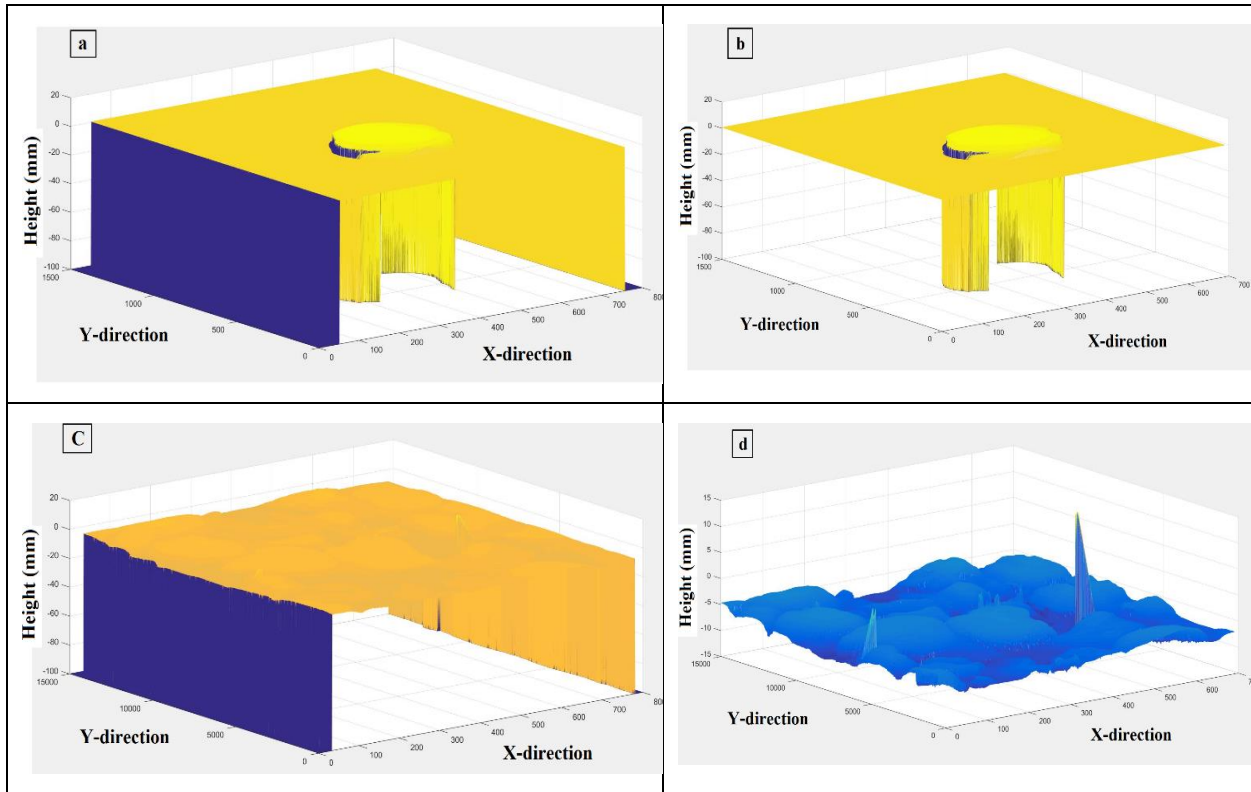


Figure 2.8 a) Unfiltered 3D scan of an aggregate, b) 3D scan of an aggregate after removing the errors at the edges, c) unfiltered 3D scan of a pavement surface, and d) 3D scan of a pavement surface after removing the errors at the edges

2.8.1. Background Color and Ambient Light

To understand how the LLS works, a basic explanation is given as to how semiconductor lasers emit light. To start, a diode consists of two semiconductors that are either n-type or p-type. The semiconductor is doped with atoms that have different electron configuration. For an n-type, the atoms are doped with allowance for extra electrons to flow freely, as there is one extra electron in the outermost energy level. The p-type is doped with an element that has a ‘hole,’ lacking an electron in the outermost energy level. When the two materials, or semiconductors, are combined into a diode, electrons flow to the holes and vice versa. An electrical power source is used to continue this interchange of holes and electrons with the use of current. At the junction of the

semiconductors, photons are released as the electrons combine with the hole. The wavelength is dependent on the semiconductor material; the different materials can have different energies from the electron-hole interaction and the photon energy is inversely proportional to wavelength. Spectral range of light is presented in Figure 2.9. For the case of the LLS, the photon has a 405-nm wavelength which is in the visible spectrum of light and it is seen as the color violet/blue to the human eye. The violet light is emitted from the LLS and then the reflection of the light from a given surface is captured by a detector. In order to evaluate the effect of background color on the accuracy of laser measurement, different color papers were placed beneath an aggregate particle (as can be seen in Figure 2.10) and tests were performed.

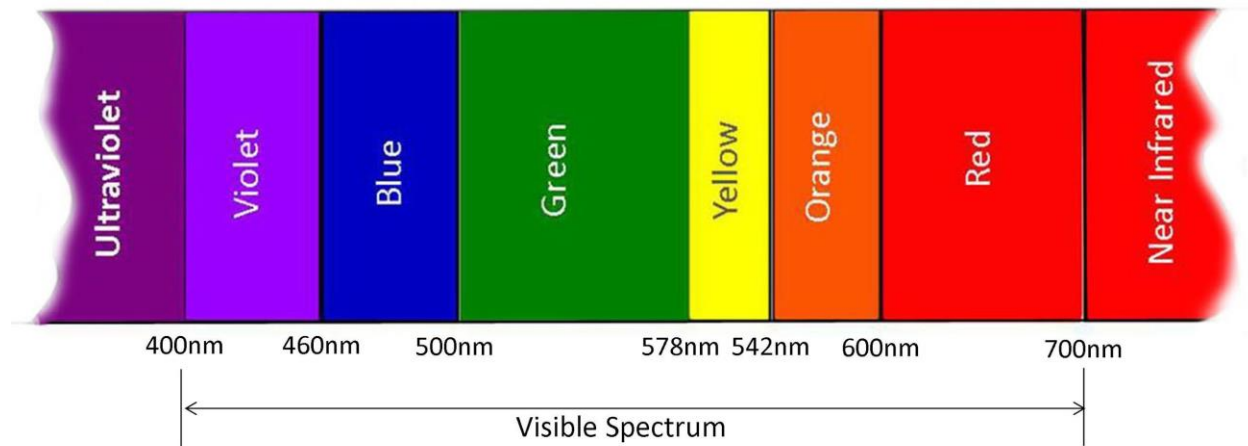


Figure 2.9 Spectral range of light (<http://karnikakapoor.blogspot.com/2016/04/weirdness-colour-spectrum.html>)



Figure 2.10 Using different background colors in measurement

The measurements were compared to each other with respect to the number of dropouts that occurred for each color paper used in the test. The results showed that the effect of background color is negligible on the data measured by the laser. This might be due to the short wavelength of the LLS photon, which is violet, compared to the other colors.

In addition, in order to detect how the scanning results differ by changing the intensity of external lights, an aggregate particle was placed on a selected background and scanned twice; in a bright

room and in a dark room with a covering box on the laser. The test was performed by comparing the number of dropouts. It is to be noted that other conditions were kept the same for both tests. It was found that in the laboratory, the laser can be operated in the room light. However, in the field, the laser must be covered by a box to avoid the direct sunlight. As provided in the LLS manual, the maximum illuminance resistance is 10,000 lux. The illuminance is used as the intensity of light that hit a surface. An illuminance of 10,000 lux corresponds to a full daylight with a non-direct sun which means that the laser should not be exposed to a direct sun. Accordingly, during the field measurement, direct sunlight could affect the measurement of the laser, since the illuminance can exceed the maximum resistance. Therefore, for all the measurements taken in the field, a covering box was used.

2.8.2. Adjusting the Settings of LJ-Navigator 2

The LJ-Navigator 2 offers several features to deal with the negative dropouts during the scanning. Several tests were performed to get a better understanding of the effect of these features on the measurement.

2.8.3. Test #1

As shown in Figures 2.11(a) and 2.11(c), an aggregate particle was placed in the scanning area of the laser and scanned in two different directions, from left to right and then from right to left, to see whether the direction of scanning affects the negative dropouts at the edges of aggregate. Figures 2.11(b) and 2.11(d) illustrates the X-Y view of the scanned aggregate. The result obtained from these two tests is that the black area (undetectable parts by the laser) occurred at the same location in two scans. Therefore, the performance of the laser is similar in both directions.

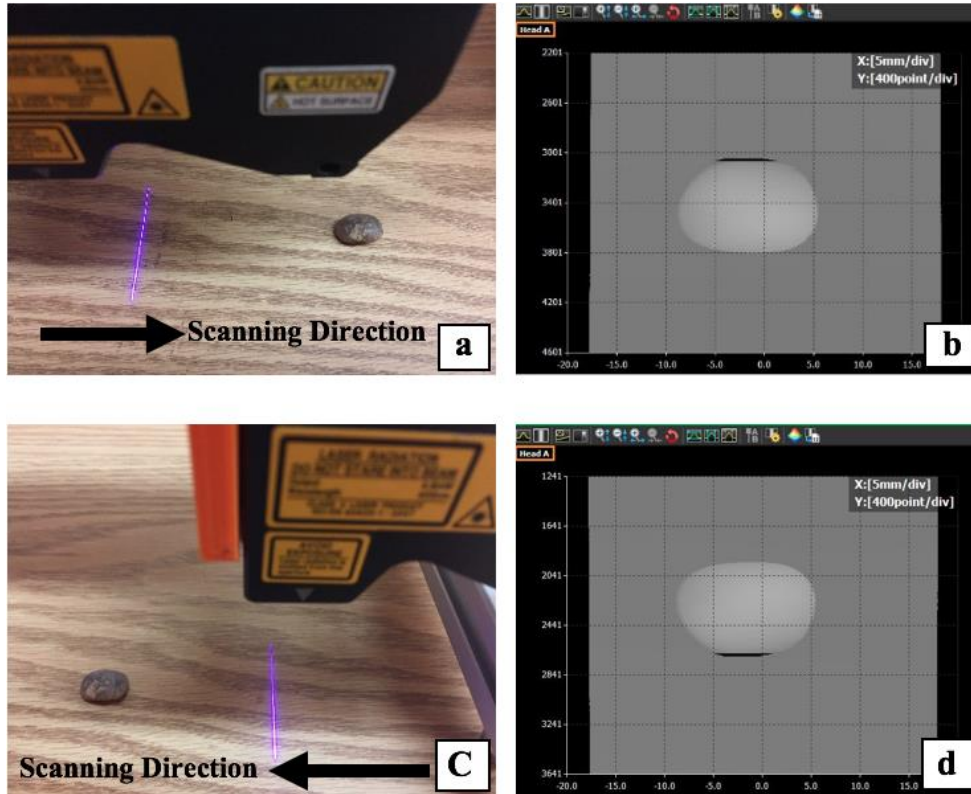


Figure 2.11 a) Scanning an aggregate from left to right, b) X-Y view of the scanned aggregate, c) Scanning an aggregate from right to left, d) X-Y view of the scanned aggregate

2.8.4. Test #2

According to the LLS manual, the negative dropouts can be considered as either dead zones or invalid data. In this test, negative dropouts were considered as dead zones. An aggregate particle was scanned three times. The variable in these three scans was the interpolation mode shown in Figure 2.12. Three interpolation modes including no interpolation, linear interpolation, vertical interpolation are offered by the LJ-Navigator 2. Figure 2.12 depicts how a profile changes by choosing the different interpolation modes. In each scan, one of these modes was selected to find how the interpolation feature influences the measurement.

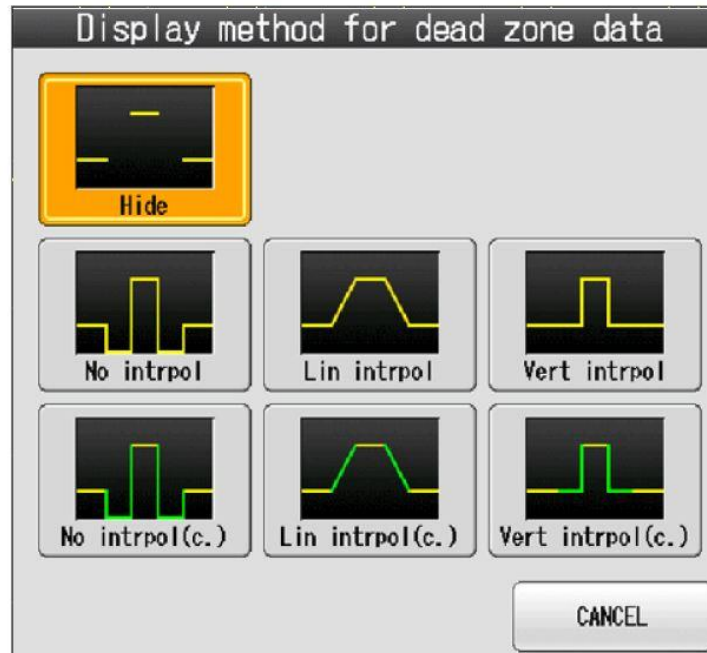
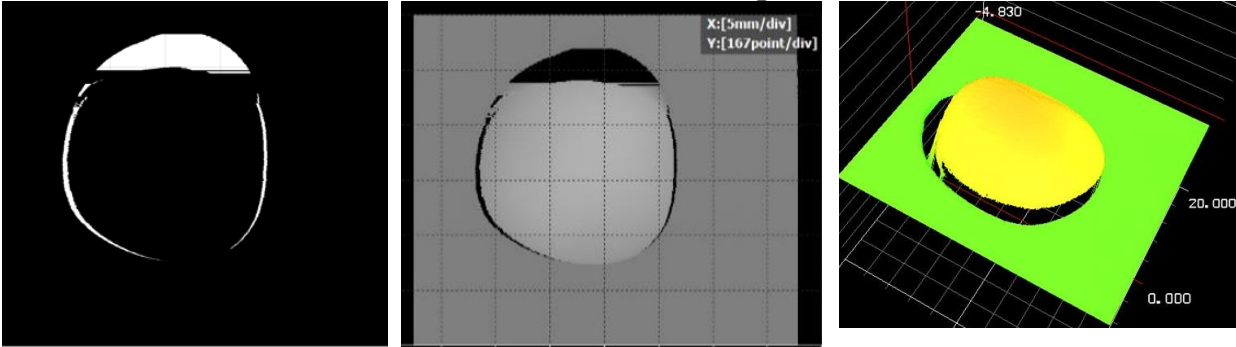


Figure 2.12 Three interpolation modes in the LJ-Navigator 2

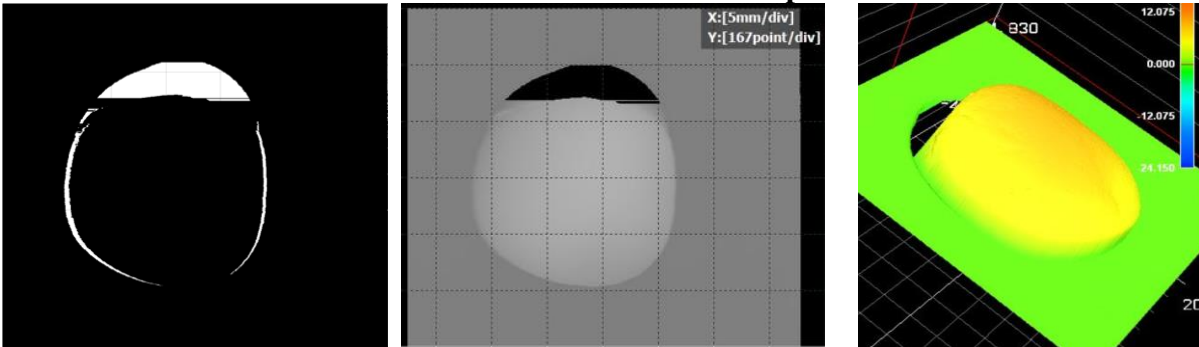
The results of the scans are provided in Table 2.3. Each row consists of three figures corresponding to each scan. The first figures from the left show the X-Y view of the outputs in the Excel file in which the white area illustrates the dead zone. The second and the third figures in each row present the X-Y view and 3D view provided in the LJ-Navigator 2. It was found that once the negative dropouts are considered as dead zones, the interpolation modes only affect the display of the data in the LJ-Navigator 2 and no change is made on the stored data in the Excel file. The number of the negative dropouts was also counted in each scan and compared to each other. These results also indicated that the interpolation features do not impact the errors in the stored data.

Table 2.3 Results of Test #2, Dead Zone and Interpolation Modes

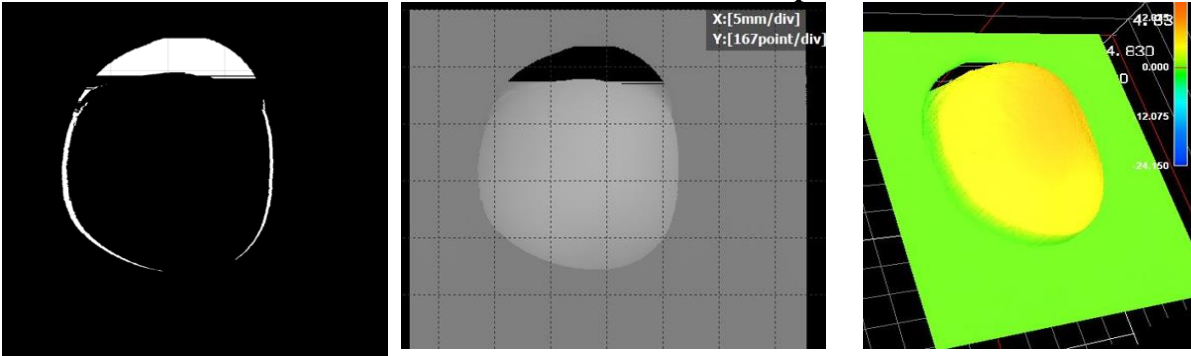
Scan 1: Dead Zone – No interpolation



Scan 2: Dead Zone – Linear Interpolation



Scan 3: Dead Zone – Vertical Interpolation



2.8.5. Test #3

In this test, negative dropouts were considered as invalid data rather than dead zones. Linear interpolation mode was also selected. Figure 2.13 shows the difference between one profile in X-direction in dead zone selection versus invalid data selection. As apparent in this figure, for invalid data, the linear interpolation feature affects the negative dropouts at the edges of the aggregate and linearly interpolates them.

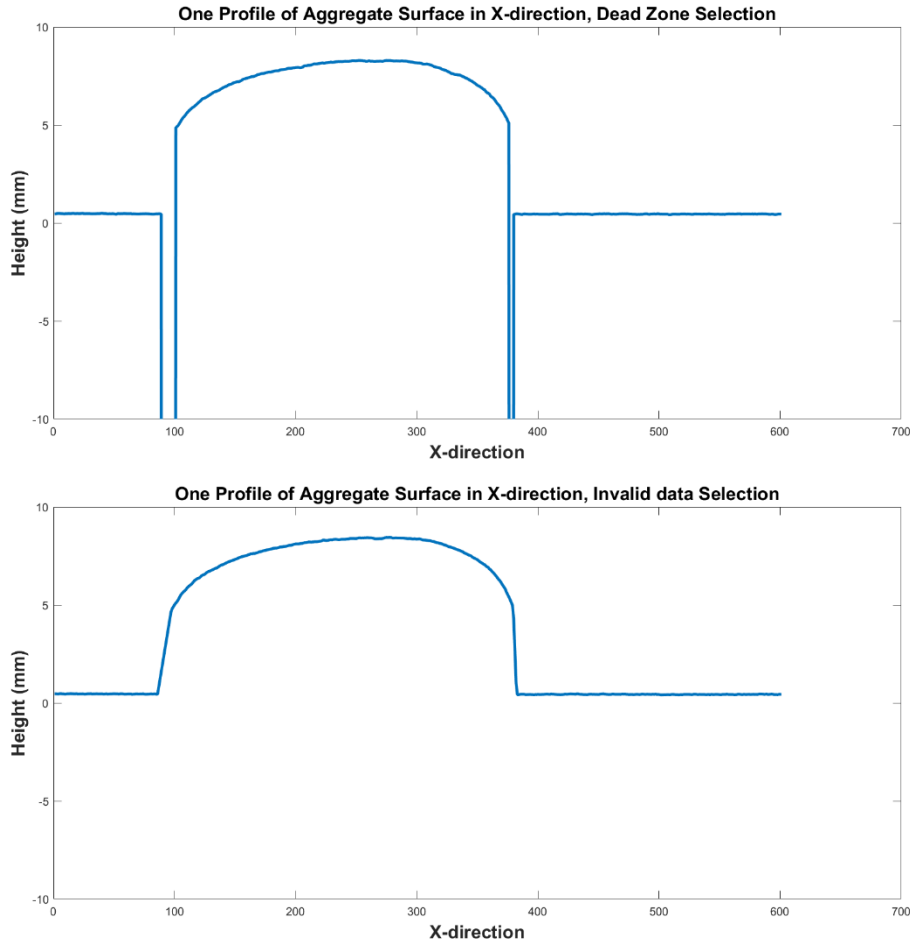


Figure 2.13 Comparing one X-direction profile of aggregate surface in dead zone and invalid modes

2.8.6. Test #4

The LJ-Navigator 2 also provides the invalid data processing feature in Y-direction. In order to apply this feature, processing time, which indicates the number of consecutive invalid data, must be selected appropriately. In this test, three numbers—10, 20, and 60—were selected. As shown in three plots of Figure 2.14, while the values 10 and 20 were less than the number of negative dropouts, 60 was an appropriate number for processing time. However, as illustrated in the last plot of Figure 2.14, the disadvantage of invalid data processing feature is that in Y-direction the negative dropouts observed in the early parts of the aggregate (black area) are completely replaced by the valid data captured from the background. However, it is not known whether the black area is related to the background or the aggregate. Therefore, this feature did not help to restore the missing parts.

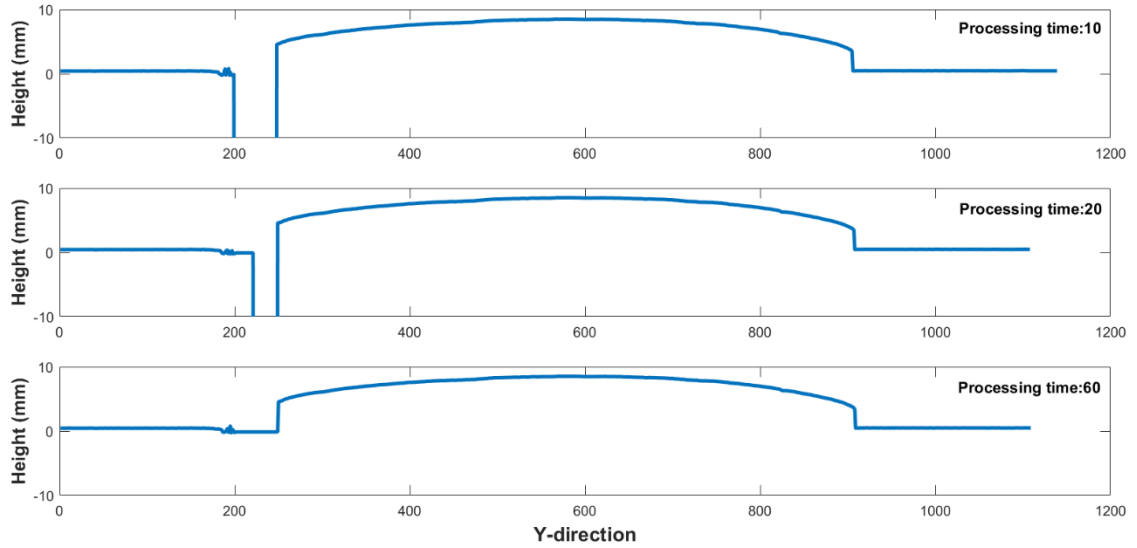


Figure 2.14 Comparing One Y-direction profile of aggregate surface in different Processing Time

2.9. Combining Two Scanned Data

To overcome the negative dropouts resulted from the triangulation system used by the LLS, the research team decided to perform two scans on the object so that the object is rotated 180 degree in each scan. Then the scanned data were merged using a code developed in MATLAB. For this purpose, a metal plate was built, as shown in Figure 2.15, and the aggregate was glued to the plate. After the first scan, the plate was rotated 180 degrees and scanned from the other direction. It should be noted that after rotation, the plate was kept in the same location to reduce additional noise in the measurements. In order to merge the two datasets, the data of the second scan was rotated 180 degrees. Then using the cross-correlation command in MATLAB, the similar parts were determined and then the two datasets were overlaid. Figure 2.16 illustrates the two datasets brought on top of each other. The white area represents the data points which are common in both datasets. The green and pink areas are related to the first and second datasets, respectively. As can be seen in this figure, there are still some black areas and it is unknown whether they are part of the aggregate or the background. Currently, the research team is getting new laser heads that will allow them to acquire the data without any processing and therefore, the unknowns related to the black areas will be avoided.

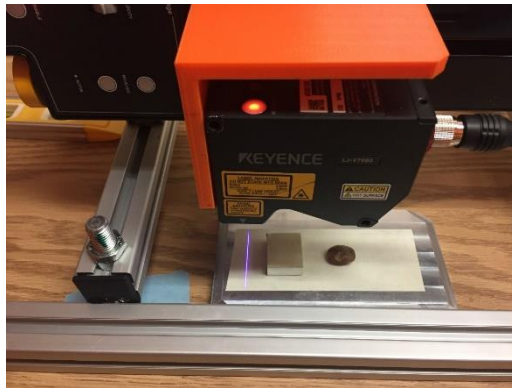


Figure 2.15 Metal plate

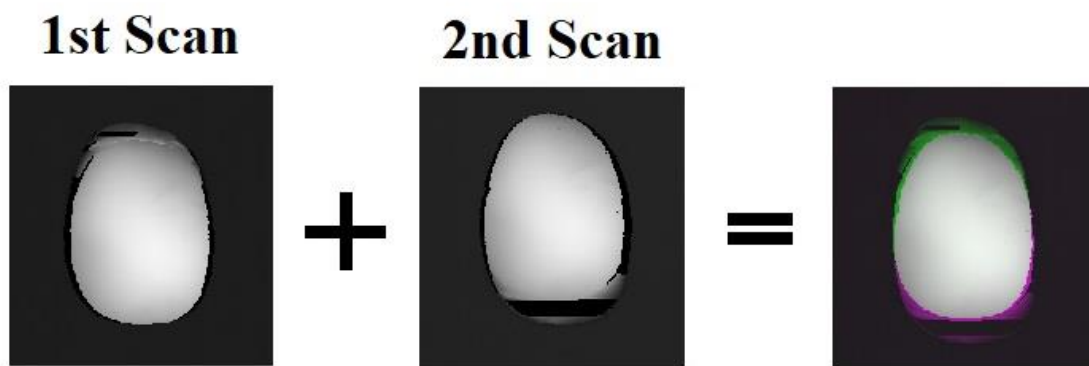


Figure 2.16 Black-and-white view of the first scan, second scan, and the two datasets on top of each other

Chapter 3. Investigating the Aggregate Texture

3.1. Introduction

The texture of aggregates has a major impact on the frictional performance of the pavements (Masad et al. 2009). Aggregates from various sources have different textures. The assessment of the aggregates texture could help to determine if the aggregates have the potential to meet the requirements of a desired pavement friction. Although several studies indicated the significant influence of micro-texture on the skid resistance of the pavement surface, the effect of different wavelengths within the range of micro-texture is not fully understood. This chapter describes the texture measurement of two different aggregate types using the developed LLS prototype. PSD analysis with two friction parameters, root mean square roughness and depth of surface roughness, were utilized to characterize the range of wavelengths that significantly contribute to the friction properties of the aggregates.

3.2. Material Preparation and Data Collection

In this study, two different types of aggregate commonly used for asphalt mixtures in Texas were obtained from two different quarries. Three particles were selected from each type of aggregate (Figure 3.1). These aggregates were provided by TxDOT's Construction Division in Austin.

The name of quarry, material type, and friction and durability test results of the selected aggregates for this research study are provided in Table 3.1. As provided in this table, group A of aggregates belongs to Surface Aggregate Classification (SAC) A and the other group was selected from SAC B. Figure 3.2 provides micro-scale view of 2.34 mm^2 of aggregates A and B, captured by microscope, in two modes: Intensity (the intensity of the reflected light for each pixel), and Range (height of each pixel) (Laurent, 2014).

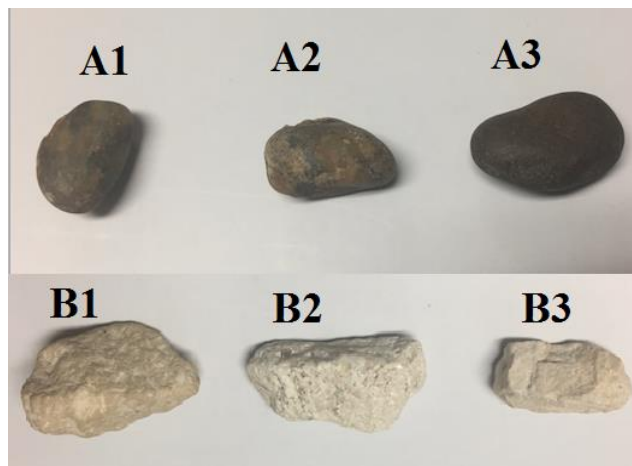


Figure 3.1 Aggregate particles

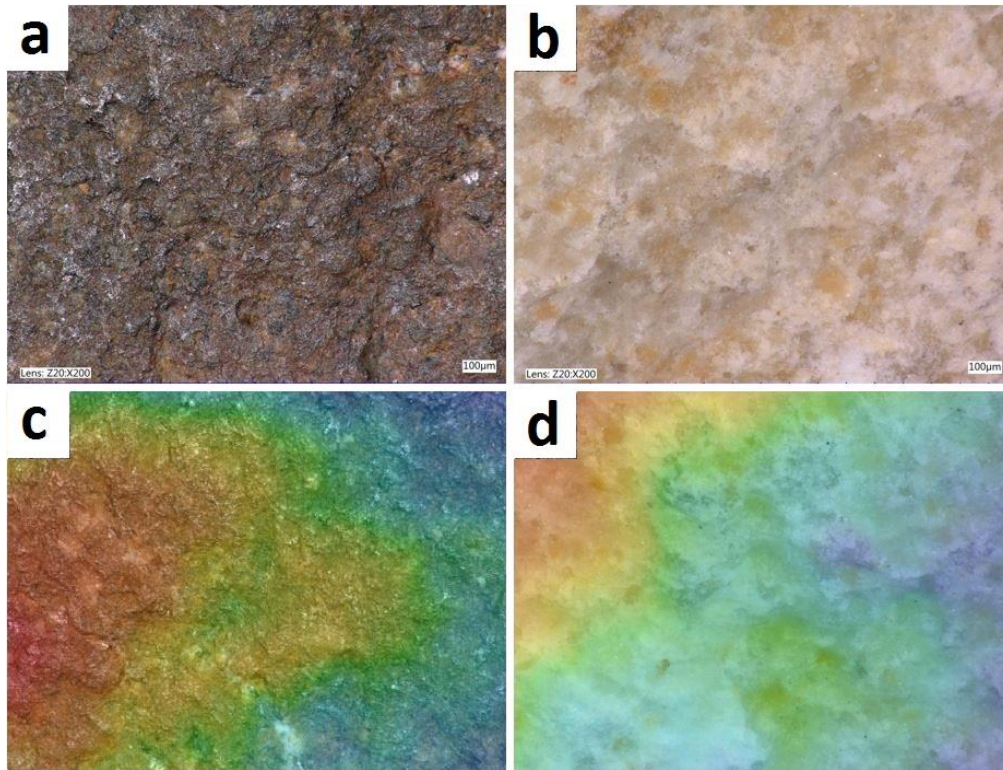


Figure 3.2 Microscopic view of texture surfaces of a) “Intensity” of aggregate A, b) “Intensity” of aggregate B, c) “Range” of aggregate A, and d) “Range” of aggregate B

Table 3.1 Aggregates Properties (BRSQC, 2016)

| Aggregate | Quarry | Used for | Material | Surface Aggregate Classification | RSLA | RSSM | | RSMD | CA-RSAI |
|-------------|--|-------------------------|--|----------------------------------|------|------|----|------|---------|
| | | | | | | HMAC | ST | | |
| Aggregate A | Big Creek Sand & Gravel, Inc. Bear Creek Pit | HMAC, Surface treatment | Crushed Siliceous and Limestone Gravel | A | 37 | 18 | 13 | 13 | 90 |
| Aggregate B | Jones Brothers - Rankin | HMAC, Surface treatment | Crushed Limestone | B | 30 | 28 | 24 | 24 | 1 |

RSLA: Rated Source Los Angles Abrasion
 RSSM: Rated Source Soundness Magnesium
 RSMD: Rated Source Micro-Deval
 HMAC: Hot Mix Asphaltic Concrete
 ST: Surface Treatment
 CA: Coarse Aggregate
 RSAI: Rated Source Acid Insoluble

The aggregates were first washed in order to remove any dust and undesirable particles. Then, the aggregate particles were oven-heated to 160°C for 24 hours followed by 4 hours of regulated air temperature and humidity to reach air-dry condition. The samples were scanned individually using the developed LLS prototype in Y-direction with resolution of 25 microns. During measurement, the optimum distance between the laser and aggregate samples was kept at 80 mm. Because the mechanism of the laser is based on projecting a light and capturing its reflection, all tests were performed in a laboratory with constant light condition to avoid any further signal noise associated to the light variation. Along with the light, the room temperature and humidity, 23°C and 45% respectively, were also kept constant during the experiments. The height profile located at the middle of each aggregate surface was selected for analysis.

3.3. Numerical Methods

A signal is a function of an independent variable, usually time or space, and it is generally used to describe physical phenomena over time or distance (Hsu, 1995; Oppenheim et al., 1998). Accordingly, the height profile captured from the aggregate surface can be considered as a signal. Signal processing theorems such as Fourier analysis and power spectral density (PSD) were employed to extract the embedded information in height profiles. Fourier analysis helps to show what wavelengths are included in a height profile and in what proportions. This section first provides a summary of types of signals and then presents explanations of Fourier Transform (FT) and PSD theorems. It is to be noted that this section focuses on time signals to explain the concepts, however the descriptions and theories can be applied to spatial signals.

Generally, signals can be categorized into the following groups.

3.3.1. Continuous and Discrete Signals

If a signal is defined as a function $x(t)$ where t is time, then the signal is continuous when t is continuous. On the other hand, if $x(t)$ happens at discrete times, $x(t)$ is classified as a discrete signal and represented by $x(t_n)$ or $x[n]$, where n is an integer (Hsu, 1995; Oppenheim et al., 1998). Figures 3.3(a) and 3.3(b) provide an example of continuous and discrete-time signals, respectively.

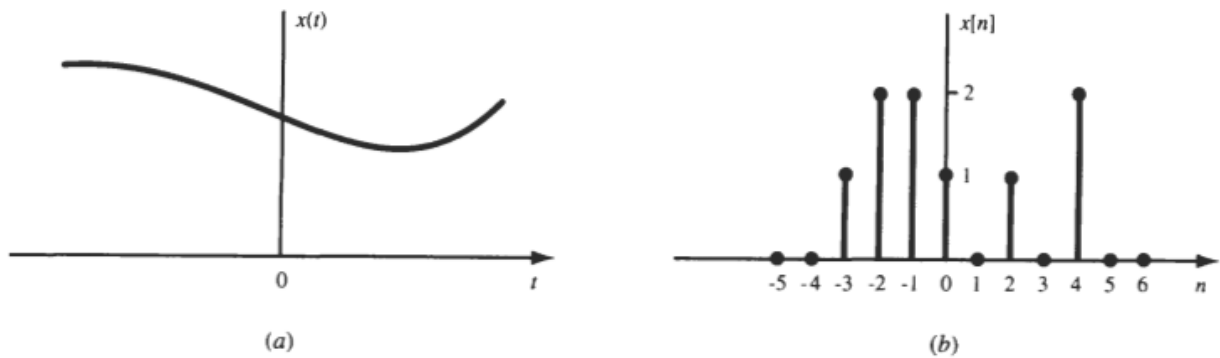


Figure 3.3 Graphical example of (a) continuous- and (b) discrete-time signals (Hsu, 1995)

3.3.2. Analog and Digital Signals

A signal $x(t)$ is analog if it happens in a continuous time interval, (t_1, t_2) (Hsu, 1995). Most of real phenomena in the world like the surface of aggregates are modeled by analog signals, but they cannot be analyzed using digital computers. To store and process analog signals using computers, they need to be converted to digital signals (Baraniuk, 2009). A digital signal is a set of discrete samples picked from a continuous signal at a given sampling interval (Hsu, 1995). Figure 3.4 shows an example of an analog and its digital samples. To digitize an analog signal, sufficient sampling is required to retain the information of that signal. In order to obtain valid data, sampling must occur at a particular time or distance called the sampling interval (Δ). The proper sampling interval is dictated by the largest frequency (Nyquist frequency) or the smallest period of interest. According to the sampling theorem, at least two samples must be considered for every cycle of the Nyquist frequency (f_N). In other words, the rate of sampling, f_s , should be at least twice of the f_N (Olshausen, 2009).

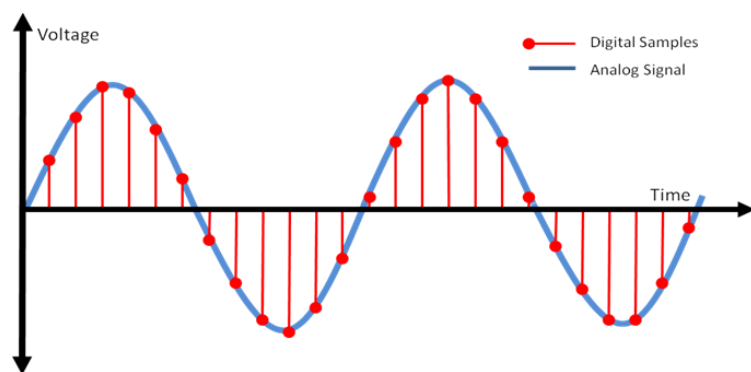


Figure 3.4 Example of analog and digital sampling (Alazartech)

3.3.2.1. Periodic and non-periodic signals

A signal $x(t)$ is periodic provided that $x(t + T) = x(t)$ for all t . Figure 3.5 provides an example of a continuous periodic function with a period T equals to 2π . A periodic signal with period T , is also periodic with $K \cdot T$, where K is an integer number. The smallest T that satisfies the above condition is called the fundamental period of $x(t)$. It is to be noted that the period in space is measured by the wavelength λ (Osgood, 2007).

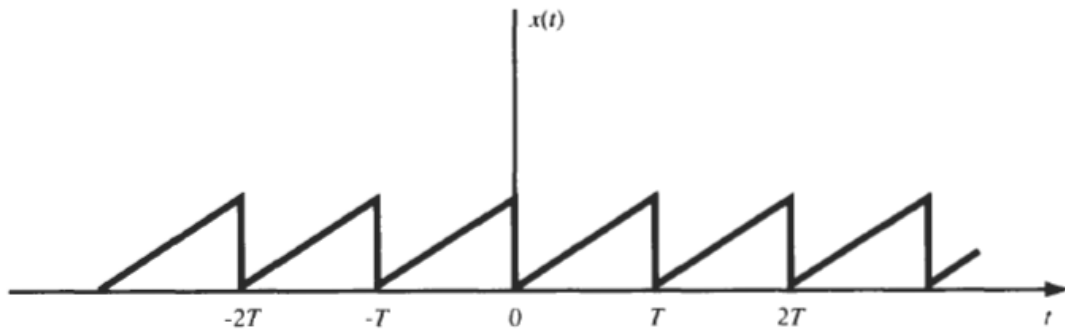


Figure 3.5 Example of a periodic continuous signal (Hsu, 1995)

Identically, a periodic discrete signal is a signal with the fundamental period N (a positive integer) that obeys the Equation 3.1. This signal is also periodic with $m \cdot N$, where m is an integer (Hsu, 1995).

$$x[n + N] = x[n] \text{ for all } n \quad \text{Equation 3.1}$$

Frequency of a signal is inversely related to the period through Equation 3.2; hence given the period, one can calculate the frequency of a signal and vice versa (Mari et al. 1999).

$$\text{For a time signal: } T = \frac{1}{f} \quad \text{Equation 3.2}$$

$$\text{For a spatial signal: } \lambda = \frac{1}{f} \quad \text{Equation 3.3}$$

where f is frequency and T (or λ) is period.

3.3.3. Fourier Transform

According to the Fourier theory, all signals could be represented as the sum of sinusoidal waves of various amplitudes and frequencies. This approach helps to find the amplitudes corresponding to those sinusoids (Karrenberg, 2013; Yoo, 2001). Generally, Fourier analysis includes two parts: 1) Fourier series, and 2) Fourier Transform (FT). The former decomposes a periodic function into the sum of sinusoidal functions, whereas the latter expands general functions that are not necessarily periodic (Putman, 2007).

This section provides the FT formulation by which a non-periodic signal can be represented in the frequency domain. Figure 3.6-top shows a non-periodic finite wave that covers the time ranges between $-T_1$ and T_1 and is equal to zero outside of that range (Hsu, 1995). A periodic signal $x_{T_0}(t)$ (as shown in Figure 3.6-bottom) can be produced by repeating $x(t)$ with an arbitrary period of T_0 such that $\lim_{T_0 \rightarrow \infty} x_{T_0}(t) = x(t)$. The FT representation of $x_{T_0}(t)$ is expressed as Equation 3.4.

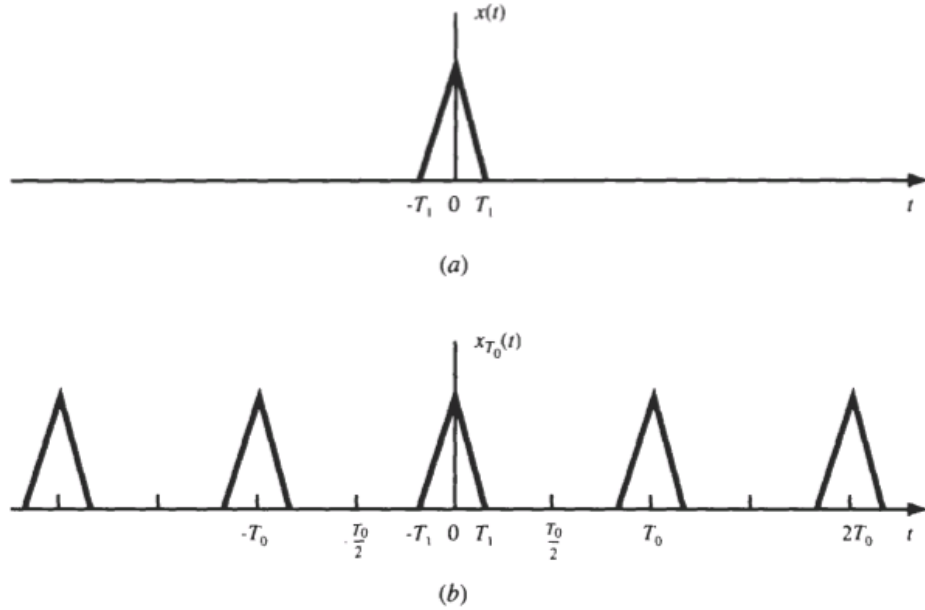


Figure 3.6 A non-periodic (top) and a periodic signal (bottom) (Hsu, 1995)

$$x_{T_0}(t) = \sum_{k=-\infty}^{\infty} C_k e^{i2\pi\left(\frac{k}{T_0}\right)t} \quad \text{Equation 3.4}$$

where T_0 is period, k only gets integers from $(-\infty, \infty)$, i is equal to $\sqrt{-1}$, and C_k is known as the Fourier coefficient and is calculated using Equation 3.5.

$$C_k = \frac{1}{T_0} \int_{-\frac{T_0}{2}}^{\frac{T_0}{2}} x(t) e^{-[2\pi i\left(\frac{k}{T_0}\right)t]} dt \quad \text{Equation 3.5}$$

Since $x(t)$ is zero outside of $(-T_1, T_1)$, the Fourier coefficient C_k for the non-periodic signal $x(t)$ can be rewritten as following:

$$C_k = \frac{1}{T_0} \int_{-\infty}^{\infty} x(t) e^{-[2\pi i\left(\frac{k}{T_0}\right)t]} dt \quad \text{Equation 3.6}$$

3.3.4. Discrete Fourier Transforms (DFT)

Consider a discrete function $x(t)$ with N points at an interval of $\Delta T = 1$. Therefore, we have a discrete function, $x[n]$, with length of $N\Delta T = N$, and a finite number of samples. Discrete Fourier series (DFT) is the Fourier transform of this sampled function that transforms N discrete points of the signal to the N equally spaced discrete frequencies.

Using the DFT, we can transform a given function from time domain to frequency domain. In the case where we have $x[n]$, DFT provides the Fourier coefficients C_k (Oppenheim et al., 2009; Orfanidis, 1995). Equations 3.7 show the DFT formulation.

$$C_k = \frac{1}{N} \sum_{n=0}^{N-1} x[n] e^{-2\pi i \left(\frac{k}{N}\right)n} \quad \text{Equation 3.7}$$

DFT is accomplished using effective computational algorithms: FFT in Matlab (Mathworks).

3.3.5. Power Spectral Density (PSD)

Power spectral density (PSD) is an analysis in the frequency domain that provides the power associated with constituent frequencies of a signal (Benbow et al., 2006; Elson and Bennett, 1995). In this case, the PSD provides the constituent wavelengths of a height profile. The PSD of a signal $x(t)$ can be calculated using the Equation 3.8:

$$PSD = \frac{1}{N} \sum_{k=0}^{N-1} |C_k|^2 \quad \text{Equation 3.8}$$

where N is the total number of Fourier frequencies and C_k is the Fourier coefficients of the signal $x(t)$.

3.3.6. Root Mean Square Roughness and Depth of Surface Smoothness

Two parameters—the root mean square roughness (Rq) and the depth of surface smoothness (Rp)—were considered as quantitative measurement of aggregates surface friction. A research study conducted by Cafiso and Taormina found that there was a good correlation between these two parameters and surface friction (Cafiso and Taormina, 2007). Rq and Rp (calculated by Equations 3.9 and 3.10) are two statistical indicators obtained from the height profile of the aggregate surface and found to have significant correlation with the British Pendulum Number (BPN), which is widely used to measure pavement surface friction (Cafiso and Taormina, 2007).

$$Rq = \sqrt{\frac{1}{N} \sum (Z_i - \bar{Z})^2} \quad \text{Equation 3.9}$$

$$Rp = \frac{1}{N} \sum_i (Z_{max} - Z_i) \quad \text{Equation 3.10}$$

where Z_i is the generic ordinate, \bar{Z} is the average of Z_i values, Z_{max} is the maximum Z value, and N is the number of points.

The PSD parameters and height profile parameters were calculated for all aggregate particles to study the effect of the aggregate's micro-scale texture on its surface friction.

3.4. Result and Discussion

3.4.1. Effect of Orientation

In principle, aggregates tend to randomly arrange within the pavement surface layer. Hence, studying the aggregates' characteristics associated with surface texture using PSD plots might be affected by aggregates' orientations. To investigate the effect of orientation, aggregate A1 was scanned in four different directions ranging from 0° to 270° with an interval of 90° , as shown in Figure 3.7. The black areas in Figure 3.7 are the missing data in which the camera was not able to detect the laser line reflected from the aggregate surface specifically in the edges. For the texture measurement, these black areas did not have an effect on the results. Subsequently, the data were analyzed and the PSD values were plotted with respect to wavelengths in Figure 3.8. This figure shows that the PSD plots of different orientations cannot be differentiated and that all follow a similar pattern, so it was concluded that the orientation of aggregate particles does not have a significant effect on PSDs. These results are consistent with the outcomes of a study conducted by Wang et al., which indicated that the influence of aggregate orientation in profile images is negligible (Wang et al., 2005).

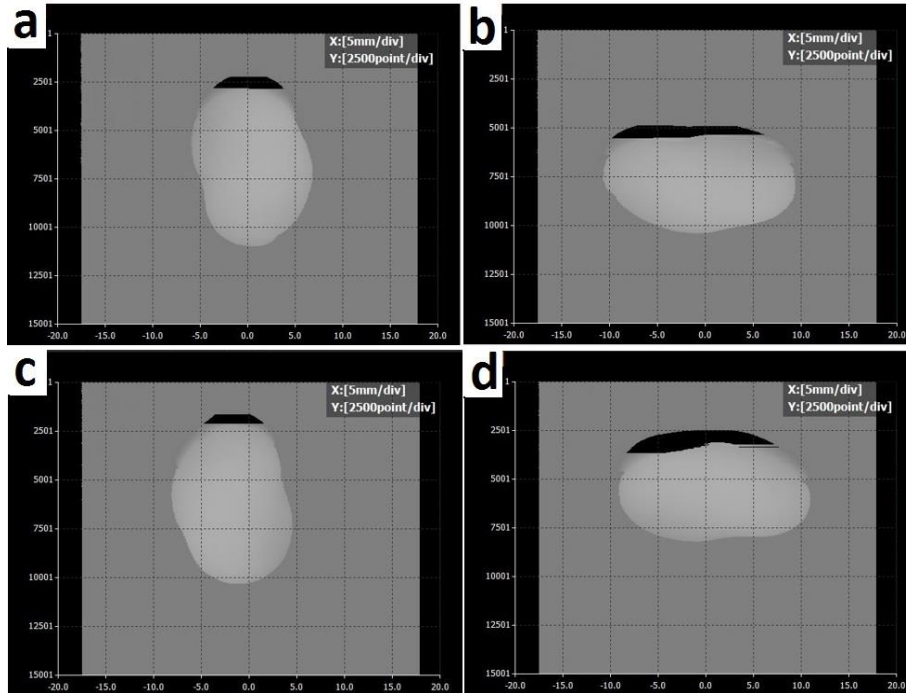


Figure 3.7 Scan of A1 in different angles a) 0° , b) 90° , c) 180° , and d) 270°

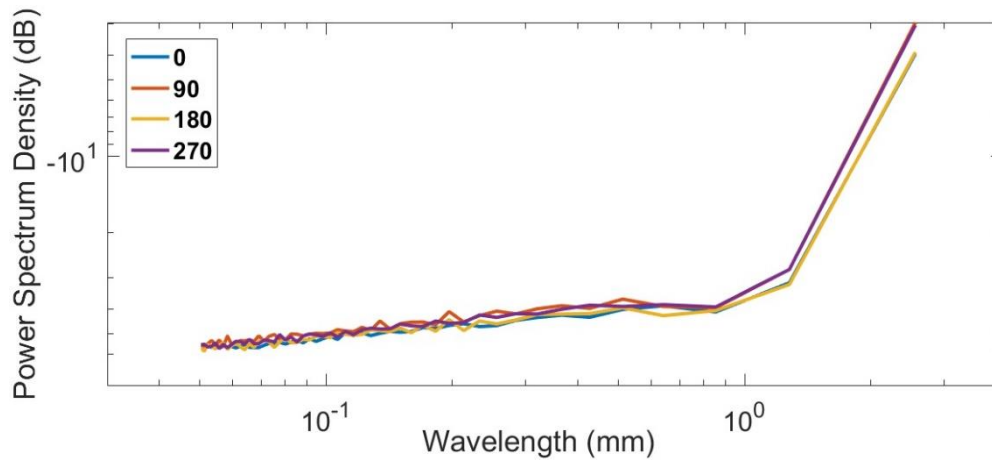


Figure 3.8 PSD of Aggregate A1 in different angles

3.4.2. Comparison of PSD Results

Figure 3.9 presents the PSD of two aggregate groups: A and B. According to this figure, the PSD values of aggregates within each group are similar in the first decade of micro-texture. Slight differences were observed in the first decade of macro-texture, which can be due to size variation of particles. These results suggest that the PSD of the aggregates in the first decade of micro-texture significantly depends on the mineralogical properties of the aggregates. Therefore, it can be concluded that aggregates obtained from the same source behave similarly in the first decade of micro-texture.

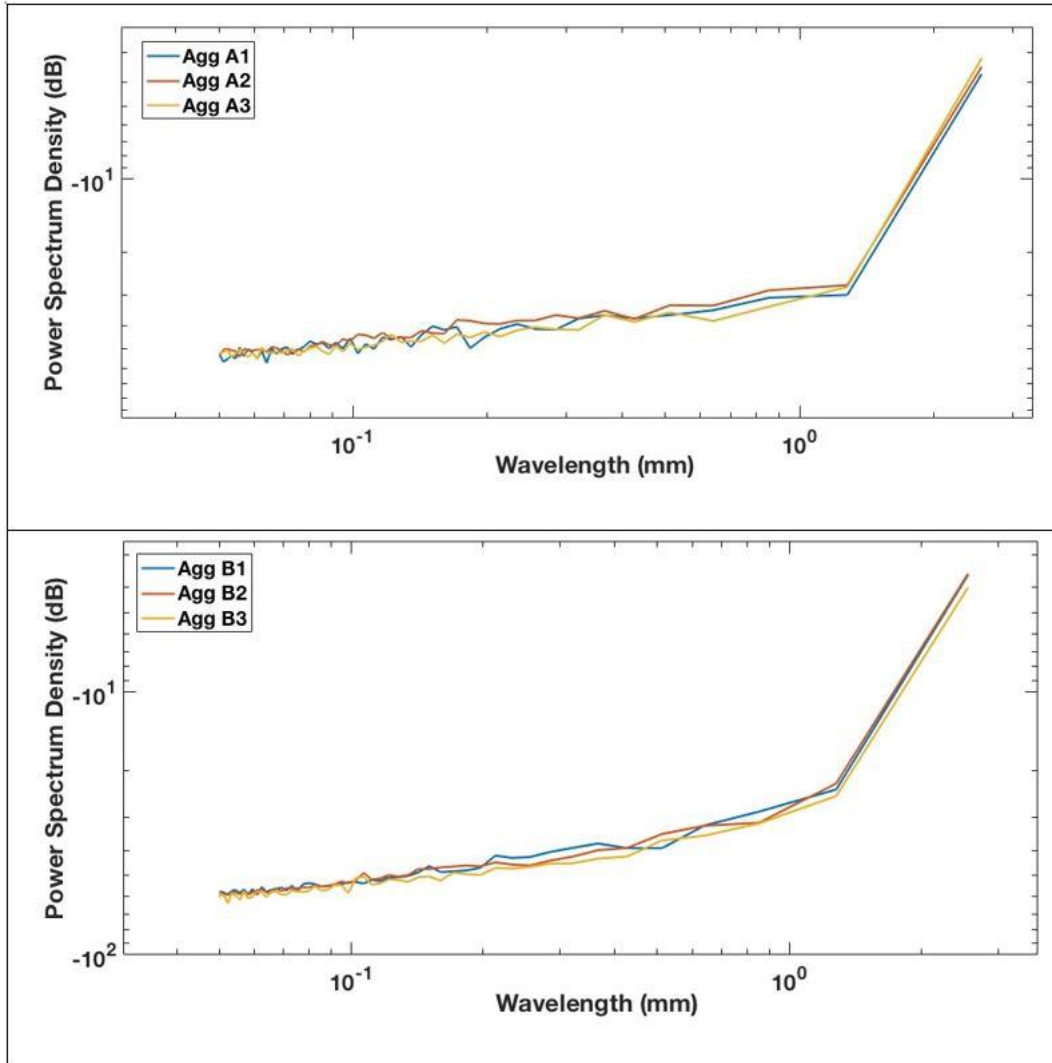


Figure 3.9 Comparison of PSD values of all aggregates

3.4.3. Paired t-test

To better quantify the aggregates' surface characteristics that contribute to the texture, two levels of wavelengths (first decade of micro-texture and first decade of macro-texture) were broken into smaller sub-bands so that the aggregates could be compared and analyzed in each sub-band in terms of their PSD values. For this purpose, the paired t-test was used. Table 3.2 provides the wavelength range of each sub-band along with the results of its paired t-test. The null hypothesis was that there is no statistical difference between the mean PSD values of aggregate A and aggregate B. According to the paired t-test results, the PSD data for aggregates in all micro-texture sub-bands can be differentiated; however, the test failed in the macro-texture sub-bands, indicating that the PSD in those sub-bands could not be differentiated. Hence, the macro-texture data were eliminated and the micro-texture data were used for further investigation.

Table 3.2 Sub-Bands of Classification of Wavelengths

| Sub-band | Range (mm) | t stat | P-value | Possibility of Differentiation |
|-----------------------------------|-------------------|---------------|----------------|---------------------------------------|
| First part of micro-texture (L1) | 0.05 – 0.075 | 19.9 | 0.00 | Yes |
| Second part of micro-texture (L2) | 0.075 – 0.1 | 25.6 | 0.00 | Yes |
| Third part of micro-texture (L3) | 0.1 – 0.25 | 11.2 | 0.00 | Yes |
| Fourth part of micro-texture (L4) | 0.25 – 0.5 | 6.54 | 0.002 | Yes |
| First part of macro-texture (L5) | 0.5 – 1.0 | 1.44 | 0.29 | No |
| Second part of macro-texture (L6) | 1.0 – 2.56 | -1.46 | 0.38 | No |

3.4.4. Evaluation of Root Mean Square Roughness and Depth of Surface Smoothness

The spatial signals captured with the LLS from the aggregate's surface texture were processed using band-pass filters in order to separate the micro-texture components. The profiles in the frequency domain were cut off between the wavelengths 0.05 to 0.075 mm, 0.075 to 0.1 mm, 0.1 to 0.25 mm, and 0.25 to 0.5 mm. These cut-off wavelengths were selected based on the defined sub-bands in Table 3.2 for the first decade of micro-texture. The filtered profiles were subsequently used to compute the texture parameters R_q and R_p at different levels of micro-texture. As an example, Figure 3.10 shows the height profile of aggregate A1 along with the four filtered profiles that were used to calculate the R_q and R_p values.

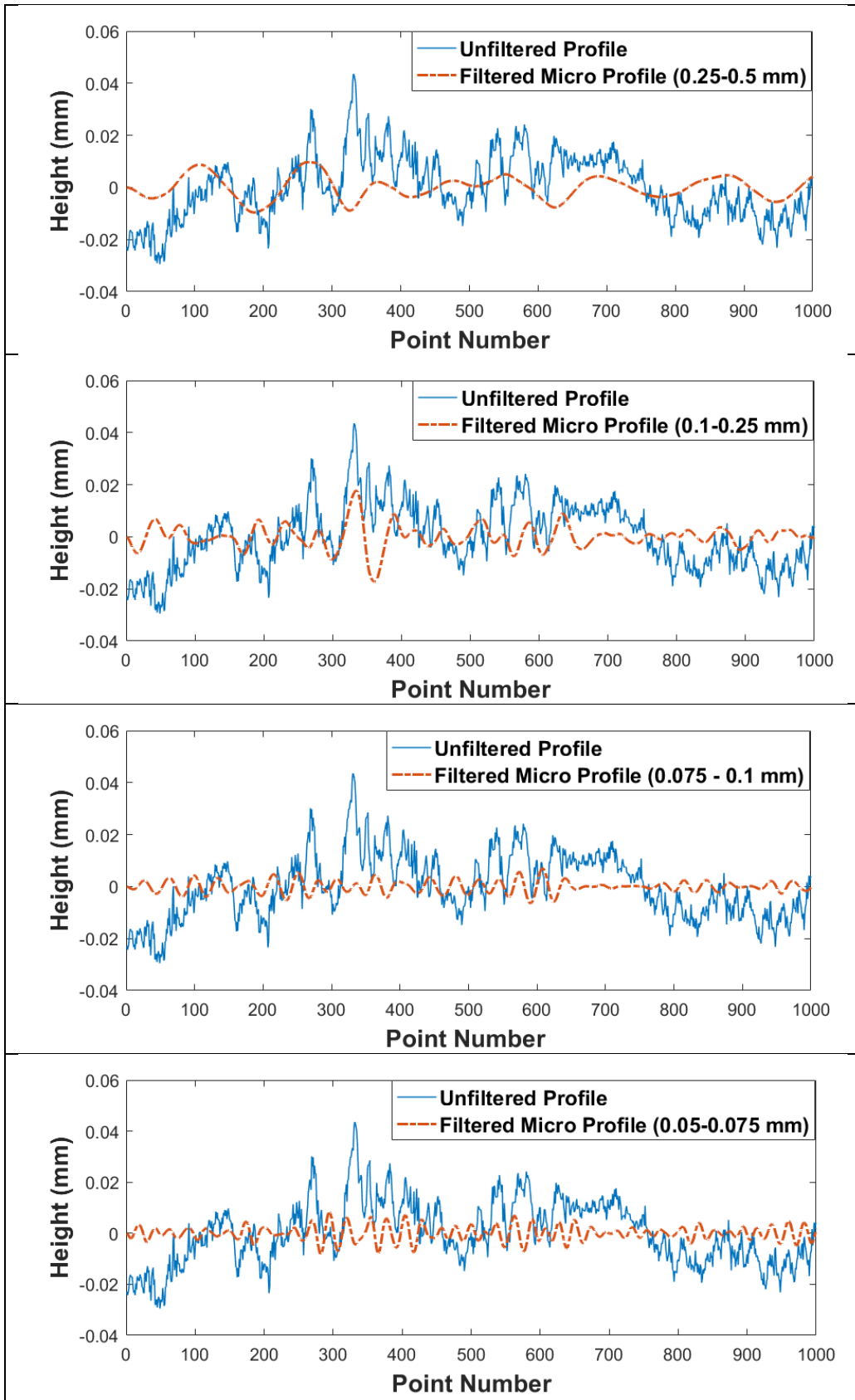


Figure 3.10 The profile of aggregate A1 with the micro-scale filtered profiles

Figures 3.11 and 3.12 show the texture parameters R_q and R_p calculated in different sub-bands (L1 through L4). As these figures demonstrate, the R_q and R_p values of aggregate type A is significantly higher than those in aggregate type B in all sub-bands except L4 (0.25-0.5 mm). These findings can be interpreted to indicate that the aggregate type A has higher friction, which is consistent with the findings arising from the PSD plots. The difference between the R_q and R_p values is more significant in sub-bands L1 (0.05-0.075 mm), L2 (0.075-0.1 mm), and L3 (0.1-0.25 mm), potentially suggesting that lower wavelengths in surface micro-texture have higher impact on the surface friction behavior of aggregates.

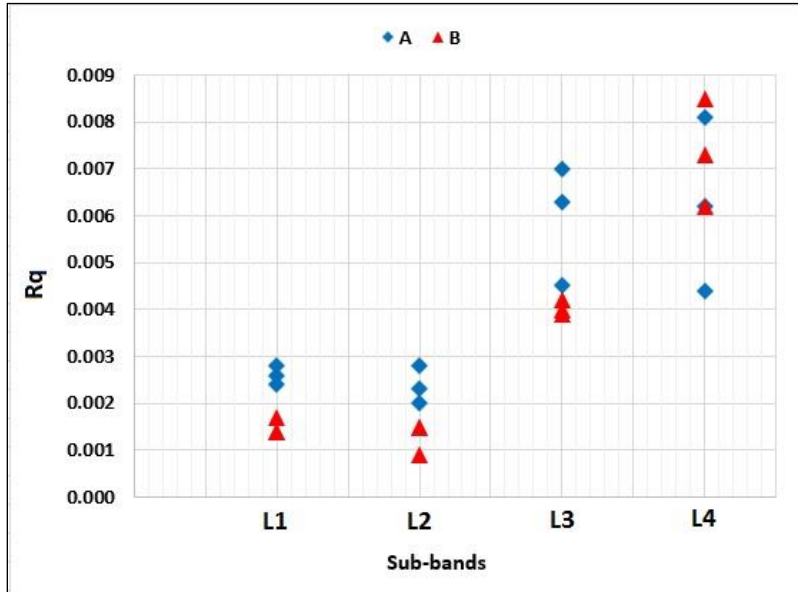


Figure 3.11 Root mean square roughness values in different sub-bands of wavelengths

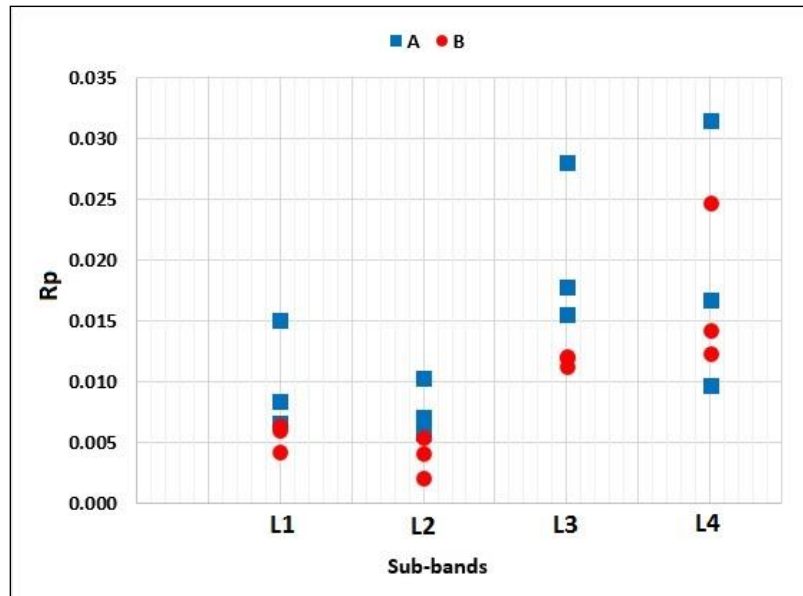


Figure 3.12 Values of depth of surface smoothness in different sub-bands of wavelengths

Table 3.3 provides a comparison between the texture parameters used in this study to differentiate aggregates in different ranges of wavelength. According to the table, the results of PSD, Rq, and Rp were consistent only in the wavelength range of 0.05 to 0.25 mm. It can be concluded that this range has the most effect on the aggregate surface texture. The LLS has demonstrated its ability to differentiate between the micro-texture of the different aggregates, and therefore has the potential to be incorporated into the SAC classification to assess the friction potential of the aggregate particles.

Table 3.3 Side-by-side Comparison of Texture Parameters in Different Wavelength Ranges

| Texture Parameters | Wavelength Range (mm) | | | | | |
|--------------------|-----------------------|-------------------|------------------|------------------|-----------------|------------------|
| | Micro-texture | | | | Macro-texture | |
| | L1 (0.05-0.075) | L2 (0.075-0.1) | L3 (0.1-0.25) | L4 (0.25-0.5) | L5 (0.5-1.0) | L6 (1.0-2.56) |
| PSD | ✓ | ✓ | ✓ | ✓ | X | X |
| Rq | ✓ | ✓ | ✓ | X | NA | NA |
| Rp | ✓ | ✓ | ✓ | X | NA | NA |

Chapter 4. Pavement Friction and Texture Correlation

4.1. Introduction

Understanding the texture-friction relationship is valuable for transportation agencies and engineers for proper pavement maintenance and better design of asphalt mixtures, especially when higher skid resistance is needed. A few studies have been conducted in this regard, but the effects of pavement texture on the friction produced at the pavement surface are still not fully understood. Hence, in this study, the researchers used field collected data of pavement friction and texture to develop friction-texture relationships appropriate for Texas conditions.







4.1.1. Measurement of Skid Resistance





There are three main skid resistance measuring principles: longitudinal friction coefficient (LFC), transverse, and stationary or slow-moving (Descornet et al., 2006; Do and Roe, 2008). The LFC measurement principle aims to measure friction when a vehicle is traveling forward in a straight line. When the brakes are applied, both the angular velocity of the wheel and the overall velocity of the vehicle decrease. When the braking force on the wheels is too strong, the wheels are “locked” and consequently slide over a surface. LFC measurement devices have slip ratios that simulate the wheel slipping process when a wheel slides over a surface. More specifically, the slip ratio compares the vehicle’s velocity to the angular velocity of the wheel. When the slip ratio is 0, the angular velocity of the wheel is the same as the velocity of the vehicle (i.e., no slip between wheel and surface). When the slip ratio is 1, there is no angular velocity in the wheel (i.e., wheel is fully locked and slides over the surface). LFC devices can have either a fixed or a variable slip ratio (Kane et al., 2013; Do and Roe, 2008).

The stationary or slow-moving measurement principle is used in compact devices usually found in the laboratory or still testing. One such device uses a pendulum arm; others, such as the DFT, use a rotating head. Both devices use rubber sliders that use the surface friction to slow down the pendulum or the rotating head (Descornet et al., 2006; Do and Roe, 2008; Andriejauskas et al., 2014).

Table 4.1 summarizes LFC measurement devices commonly used around the world. LFC devices can measure between 5 and 140 km/h (3 and 87 mph) and can come in the form of compact trailers or large-capacity trucks. LFC devices use a watering system, requiring vehicles to carry a water tank for testing purposes. Transverse friction measurement devices are usually larger, more expensive, and can take measurements for longer distances since greater water capacity increases maximum measurement distance. While inexpensive and easy to use, stationary or slow-moving devices must be operated manually (Andriejauskas et al., 2014).

Table 4.1 Comparison of the LFC Measuring Devices (Descornet et al., 2006; Do and Roe, 2008; Andriejauskas et al., 2014)

| Device Name | Theoretical water film thickness (WFT), Speed, Tire type, Measurement interval (Interval) | Assembly | Device Picture |
|-------------|--|--|---|
| ADHERA | TWFT: 1 mm Speed: 40–120 km/h Tire type: Smooth PIARC tire 165R15 Interval: 20 m Country/Countries of Use: France | Assembly: Trailer that can be hooked up to vehicle Commercially Available: No |  |
| BV-11 | TWFT: 1 mm Speed: 20–160 km/h [C] Tire type: Trelleborg tire T49 Interval: 20 m Country/Countries of Use: England, Sweden, and Finland | Assembly: Trailer that can be hooked up to vehicle Commercially available: Yes |  |
| Grip-Tester | TWFT: 0.5 mm Speed: 5–100 km/h Tire type: Smooth ASTM tire, 254 mm diameter Interval: 10 or 20 m Country/Countries of Use: United States, United Kingdom, and others | Assembly: Trailer that can be hooked up to vehicle. Commercially available: Yes |  |
| ROAR DK | WFT: 0.5 mm Speed: 60–80 km/h Tire type: ASTM 1551 Interval: 5m + Country/Countries of Use: Denmark | Assembly: Trailer that can be hooked up to a vehicle Commercially available: No |  |
| ROAR NL | TWFT: 0.5 mm Speed: 50–70 km/h Tire type: ASTM 1551 Interval: 5–100 m Country/Countries of Use: Netherlands | Assembly: Three-axle tanker truck with two measuring systems mounted at the rear of the chassis. (Tank capacity is about 12,000 liters.) Commercially available: No |  |
| RWS NL | TWFT: 0.5 mm Speed: 50 – 70 km/h Tire type: PIARC smooth 165 R15 Interval: 5 – 100 m Country/Countries of Use: Netherlands | Assembly: Trailer that can be hooked up to a vehicle. Commercially Available: No |  |

| Device Name | Theoretical water film thickness (WFT), Speed, Tire type, Measurement interval (Interval) | Assembly | Device Picture |
|------------------|---|---|---|
| Skiddometer BV-8 | TWFT: 0.5 mm Speed: 40–80 km/h TT: AIPCR ribbed, 165 R15, with four longitudinal grooves Interval: 30–50 m Country/Countries of Use: Sweden | Assembly: Trailer that can be hooked up to a vehicle Commercially available: Yes |  |
| SRM | TWFT: 0.5 mm Speed: 40–80 km/h TT: AIPCR ribbed, 165 R15, with four longitudinal grooves Interval: 20 m Country/Countries of Use: Germany | Assembly: The test wheels are mounted on the back of a tanker vehicle at the approximate location of a vehicle tire paths. Commercially available: No |  |
| TRT | WFT: 0.5 mm Speed: 40–140 km/h Tire type: Smooth ASTM Interval: Typically, 20 m Country/Countries of Use: Czech Republic | Assembly: The measuring equipment is under a specially equipped vehicle Commercially available: No |  |
| SRT-3 | WFT: 0.5 mm Speed: 30–90 km/h Tire type: Tire with thread (200kPa) Interval: 100 m Country/Countries of Use: Poland | Assembly: Trailer that can be hooked up to a vehicle Note: SRT-3 is more sensitive to micro-texture changes than to macro-texture changes. Commercially Available: No |  |
| IMAG | WFT: 1.0 mm Speed: up to 140 km/h Tire type: PIARC smooth profile tire Interval: N/A Country/Countries of Use: France, Germany, and Poland | Assembly: Trailer that can be hooked up to a vehicle Commercially available: Yes |  |

Among the measurement devices presented in Table 4.1, the Grip-Tester was selected because it showed the most promise for measuring pavement friction due to its wider range of test speed, better repeatability and reproducibility (depending on the operating speed), greater efficiency in water usage, and commercial availability. The Grip-Tester is a friction-measuring trailer that uses a fixed slip wheel to simulate anti-lock braking on a wet road surface. This is achieved by the Grip-Tester having three wheels: two have patterned treads and are connected by a drive axle, while the third is a smooth tread tire. The drive axle, connecting the two drive wheels, has a 27-tooth

sprocket; it is connected by a transmission chain to the measuring wheel that has a 32-tooth sprocket (Thomas, 2008). The difference in sprocket teeth creates a 15% continuous slippage on the measurement tire. To create wet road conditions, a watering system supplies a constant water thickness specified by the user to the measuring wheel.

The axle connecting the measuring wheel outputs the dynamic friction by using strain gages to measure the horizontal drag force and vertical load force. The information is used to estimate the Grip Number (GN), or coefficient of friction, in real-time (Thomas, 2008). As shown in Equation 4.1, the GN is the ratio between the fraction of tractive drag force (F_d) and the load force (Q).

$$GN = \frac{F_d}{Q} \quad \text{Equation 4.1}$$

The Grip-Tester (Figure 4.1(a)) requires a vehicle capable of towing the trailer as well as a water tank to supply water to the measuring wheel.

Along with the Grip-Tester, the DFT was used to measure the friction of the pavement at different speeds. This piece of equipment is specified under ASTM E1911. The DFT (shown in Figures 4.1(b) and 4.1(c)) consists of a rotating disk and three rubber pads attached to the bottom of the disk. The disk is pushed by an electric motor to rotate until it reaches the target speed set by an operator. At the same time, water is applied to the pavement surface. The disk drops and the rubber pads come into contact with the wet area. Each rubber pad is loaded vertically at 11.8 N (2.65 lb). The friction force developed between pads and the pavement slows down the disk. The DFT measures the friction coefficient continuously until the disk stops completely (Huang and Pan, 2006). As provided in Equation 4.2, the coefficient of friction (μ) is the ratio between the friction force or horizontal torque force (F) and the applied vertical load on the rubber sliders of the DFT (Austroads, 2005).

$$\mu = \frac{F}{Q} \quad \text{Equation 4.2}$$

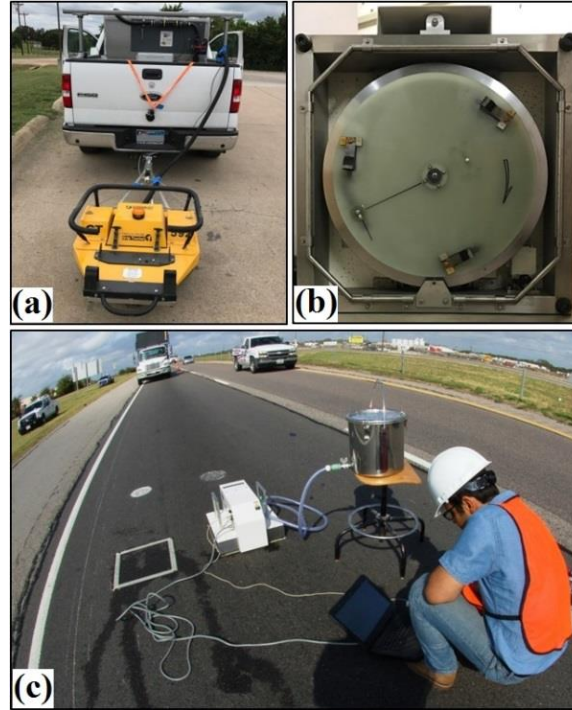


Figure 4.1 a) The Grip-Tester attached to a vehicle, b) bottom view of the DFT, and c) the DFT connected to a water tank and DCC measuring the friction at the lane center path

4.1.2. Measurement of Pavement Surface Texture

CTM is a common static method used to measure the macro-texture of the pavement surface. According to the ASTM E2157, the CTM (Figures 4.2(a) and 4.2(b)) consists of a laser-displacement sensor that rotates over a circle with a diameter of 284.5 mm (11.2 in.) and measures the profile of pavement surface texture. The profile includes 1,024 points scanned at an interval of 0.87 mm (0.034 in.). Using the instructions provided by ASTM E 1845, the measured profile then is sectioned into eight equal parts (Abbas et al., 2007; Mataei, 2016). Along with the CTM, the developed LLS prototype was also utilized to study the pavement texture.

The Mean profile depth (MPD) is calculated from the height profile obtained from both the CTM and LLS following ASTM E1845. The first step is to quantify the inclination slope of the height profile such that a regression line is calculated and then subtracted from the height profile and so the initial profile will be converted to a zero-mean profile. As a second step (Figure 4.3), the height profile is divided into two segments with the length of $\frac{L}{2}$ for which the maximum height is detected. By using Equation 4.3, MPD is calculated as the average of the two determined maximum heights.

$$MPD = \frac{\text{Max Height of 1st Segment} + \text{Max Height of 2nd Segment}}{2} \quad \text{Equation 4.3}$$

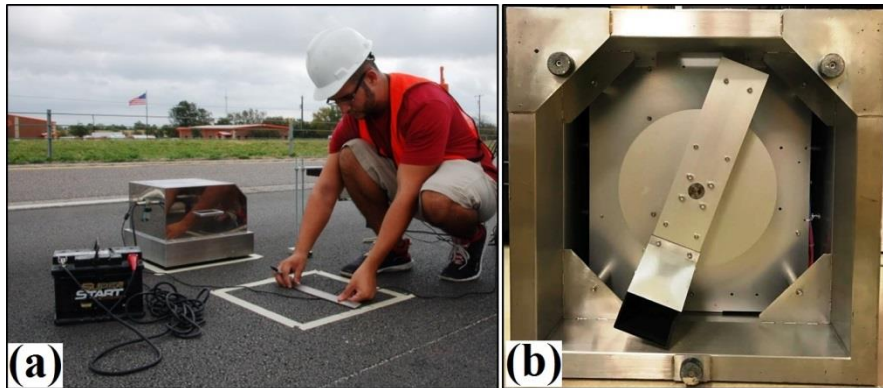


Figure 4.2 a) The CTM powered by a battery measuring the texture at the right wheel path, and b) bottom view of the CTM

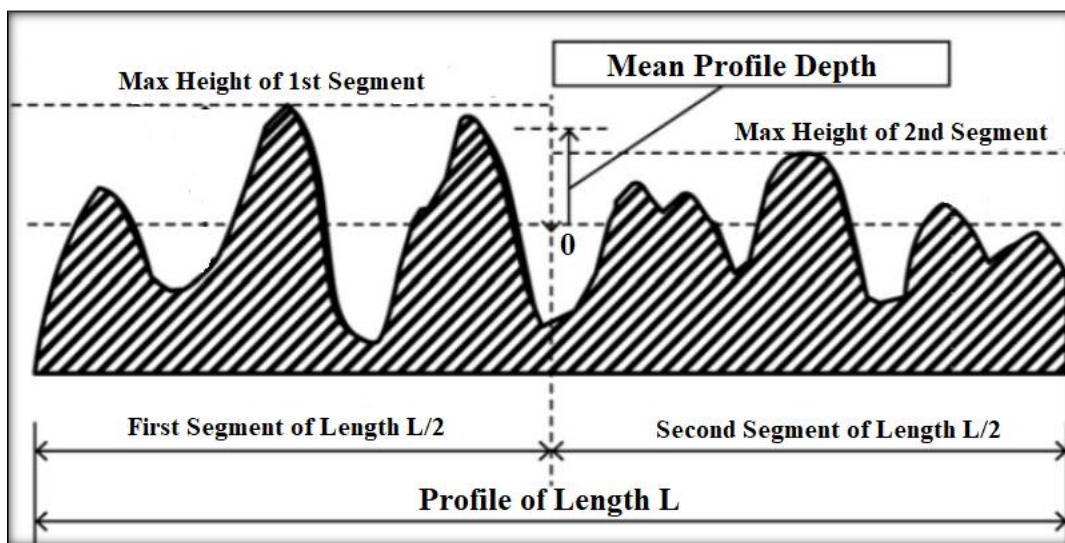


Figure 4.3 Graphical illustration of MPD calculation (26)

4.2. Data Collection

Three test sections, each more than five years old, were selected. Each section had established measurement data for the DFT, CTM, and LLS. The sections chosen provide a variety of mix designs, ensuring variation of surface texture for the test. The test sections are located in Bastrop, Bryan, and Fort Worth of Texas:

- Bastrop:
 - o Mix design: Porous Friction Course (PFC)
 - o Average annual daily traffic (AADT): 13,972
- Bryan:
 - o Mix design: Dense-Graded Type C

- o AADT: 5,843
- Fort Worth:
 - o Mix design: Dense-Graded Type D
 - o AADT: 57,385

At each location, six samples were taken: three in the right wheel path and three in the center of the lane, with a 12.5 m (41 ft) distance between the locations (Figure 4.4). Within each location, one CTM and one DFT measurements were obtained. The CTM and DFT testing followed ASTM E2157 and ASTM E1911 procedures, which state the equipment should be placed in the same location.

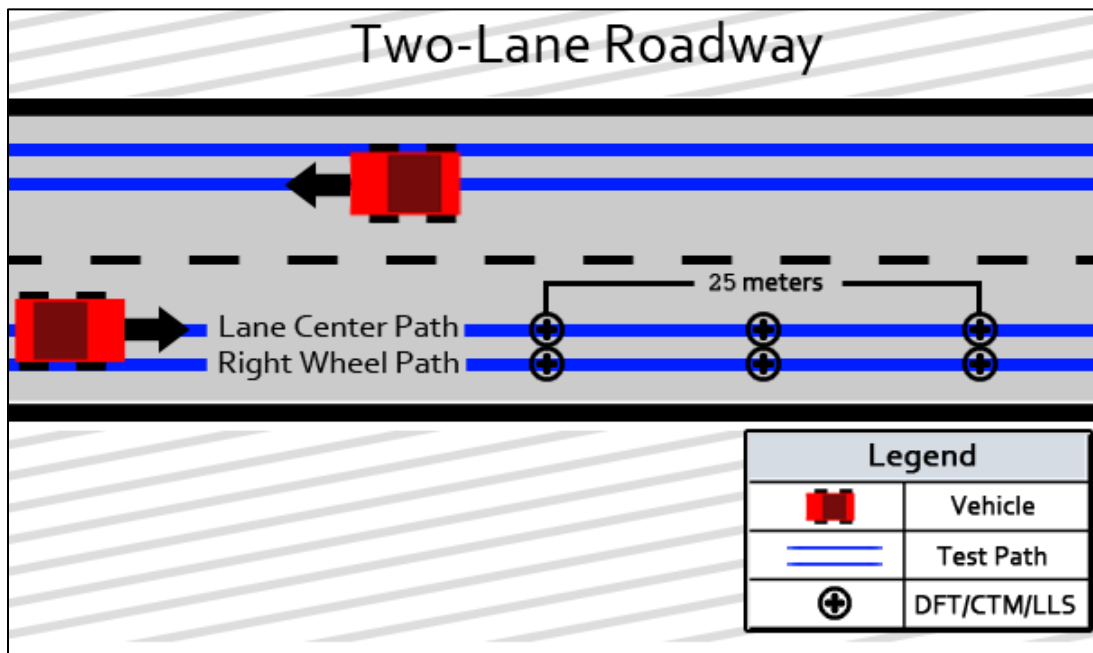


Figure 4.4 Illustration of test section and test location

To maintain consistency in the surface measurements, the LLS was placed in the same locations described for the CTM. Note, however, that these devices operate differently due to the mechanism of motion in each: the CTM measures in a circle and the LLS measures linearly. For the CTM, eight segments of 111.5 mm (4.39 in.) arcs are scanned by the laser, which results in a full circle. To ensure an equitable comparison with the CTM's measurements, the LLS was configured to scan a 120 mm (4.72 in.) length at a linear speed of 8 mm/s (0.31 in./s) with a sampling frequency of 1 kHz. The area scanned by the LLS was the same as the segment of the CTM that was parallel to the direction of traffic.

For the Grip-Tester, the test consisted of two target speeds (50 km/h and 70 km/h) to evaluate the dependency of speed on friction. The speed needs to be maintained within 5% of the target speed.

The 70 km/h (44 mph) target was selected to enable a direct comparison to the DFT equipment, which has a speed range of up to 80 km/h (50 mph).

4.3. Results and Discussions

4.3.1. Repeatability of Developed LLS Prototype

The LLS results were compared to those from the CTM to investigate the repeatability and reliability of the developed LLS. The MPD, as a surface characteristic, was calculated for all test locations. Then, single values of MPD for the right wheel path and the center were obtained by averaging the three respective samples. This was done for both LLS and CTM as graphed in Figure 4.5(a)—the -R and -C represent the right wheel path and center lane path, respectively. As this figure illustrates, the MPD values obtained by the LLS, denoted as *MPD-by-LLS*, are very close to the MPD values of CTM, denoted as *MPD-by-CTM*. There were no observable biases between the MPD values with which to draw a general conclusion.

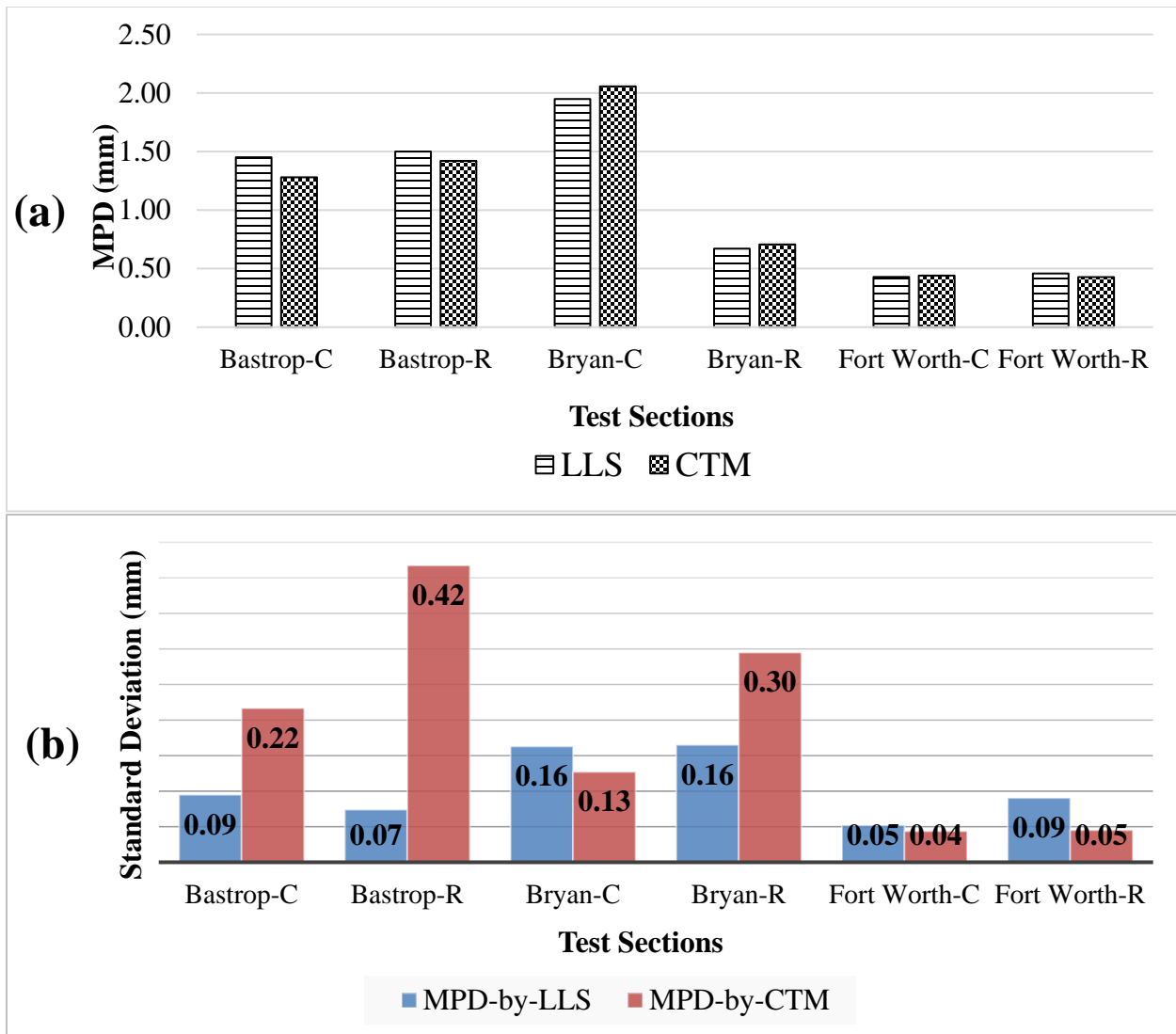


Figure 4.5 a) Comparison of mean MPD values obtained from developed LLS prototype and CTM, b) Standard deviation of MPD values measured by developed LLS prototype and CTM at six test sections

Repeatability of the developed LLS prototype was evaluated by calculating the average and standard deviation of three MPD-by-LLS and MPD-by-CTM values obtained at each test section from their respective test paths. Then, the standard deviation of each group of data was compared. For example, the three MPD-by-LLS values for the pavement surface under the right wheel path at the Bryan test section were compared to each other with respect to their standard deviation. Due to the short distance between test locations, similar texture characteristics were expected at those locations. As Figure 4.5(b) indicates, the standard deviations of MPD-by-LLS data were significantly lower than MPD-by-CTM in three test sections (Bastrop-R, Bastrop-C, and Bryan-R). Comparable MPD values were observed at the rest of the sections. According to these results, one can suggest that the developed LLS prototype is capable of providing an accurate and precise measurement of the pavement surface texture.

4.3.2. Grip-Tester Results

Figures 4.6(a) and 4.6(b) show the GN of all test locations plotted against the DFT values at two different speeds of 50 and 70 km/h (31 and 44 mph). As these figures illustrate, the GN values have a strong relationship with DFT values, with R^2 of 0.93 and 0.91 at the two different speeds. It can be concluded that this relationship is independent of the test speed.

These findings indicate that the Grip-Tester is a reliable alternative for the DFT and does not require traffic control, therefore, it is safer and more efficient. Besides, the Grip-Tester enables engineers to obtain continuous friction data over a long pavement section.

Based on the literature, no given speed has been specified by agencies to perform the test. Hence, understanding the effect of speed on GN would help researchers and practitioners interpret the friction results in different cases when the test speed is a variable. The results plotted in Figure 4.6(c) show that the GN decreased when the speed increased. This finding is reasonable but contrasts with the results of a study conducted at the University of Auckland by Wilson et al. in 2013, in which they stated that at speeds less than 75 km/h, the GN may not be affected by test speeds (27).

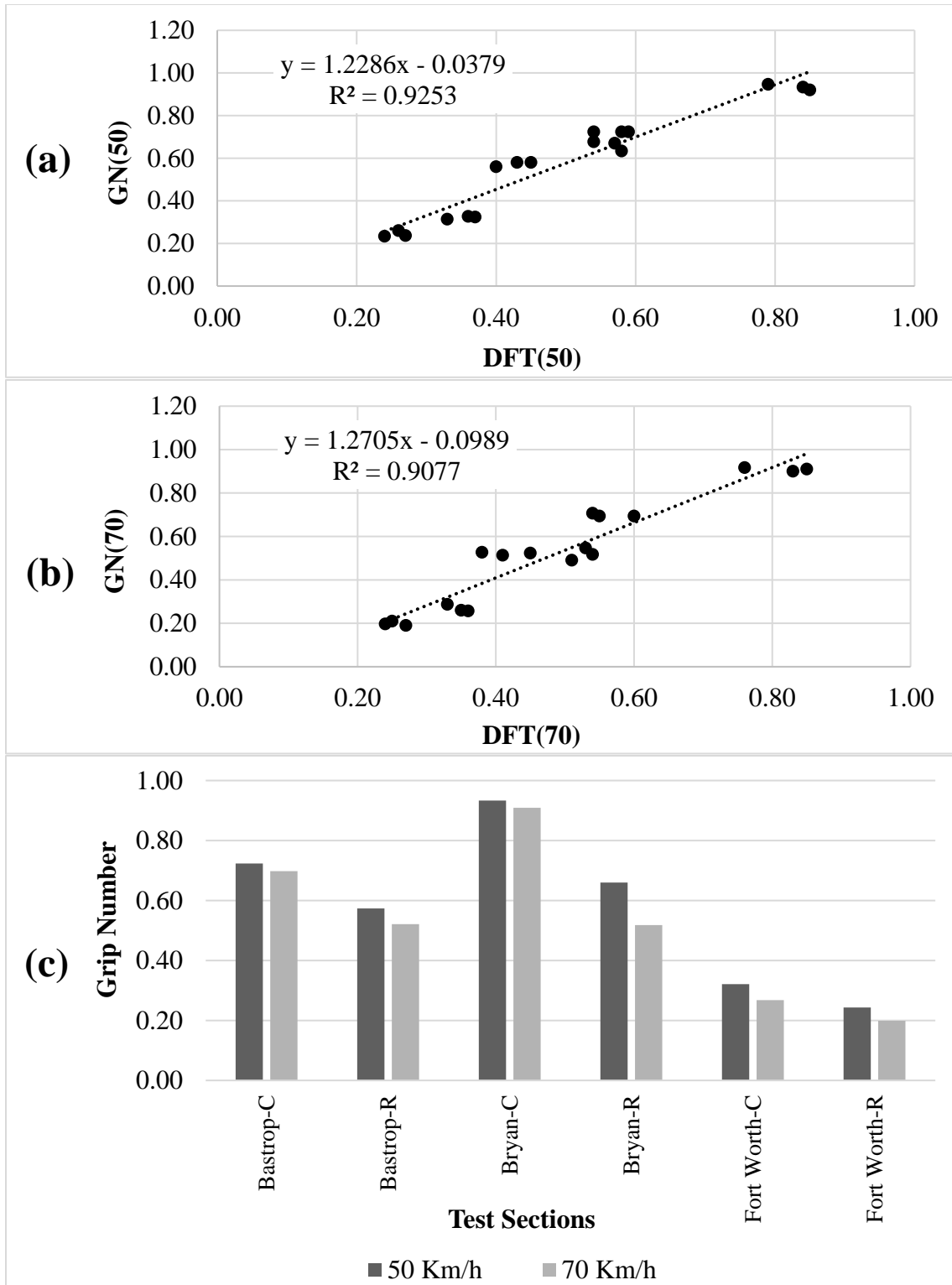


Figure 4.6 Correlation between GN and DFT values at two speeds of 50 and 70 km/h

According to Figure 4.5(a), the MPD value of the section Bryan-R, which is about 0.70 mm (0.027 in.), is lower than Bastrop-R with MPD of 1.50 mm (0.06 in.). However, interestingly, in Figure 4.6(c), the GN at Bryan-R is higher than that of Bastrop-R. It should be mentioned that, in these test locations, the water film thickness of 0.5 mm (applied by Grip-Tester) can only cover a portion of surface texture depth. The surface pavement type of the Bastrop test section is PFC; therefore, the lack of small-size aggregates results in higher MPD values. On the other hand, the mix design of the Bryan test section is dense-graded type C, which contains all ranges of aggregate size and thus results in a lower MPD value but a greater tire-pavement contact area. In this case, it can be suggested that the adhesion factor is decisive in friction.

Although a PFC mix design increases the surface MPD (and thus causes more hysteresis), PFC's design also decreases the chance of the aggregates being fully exposed and coming into contact with the tire (thus decreasing the contact area and adhesion). A smooth surface is associated with more contact area and better adhesion, but it significantly decreases the MPD that results in lower hysteresis. Therefore, the balance between adhesion and hysteresis in the pavement surface should be optimized in order to maximize the surface friction and skid resistance. This is achievable by using an appropriate mix design providing both macro-texture and micro-texture.

The lowest friction was observed in the Fort Worth test sections where the MPD values were below 0.46 mm (0.018 in.). Considering the water film thickness of 0.5 mm (0.019 in.) applied by the Grip-Tester for wetting purpose, it can be concluded that the surface texture was fully covered by water. In this case, the water trapped in the V- or U-shaped areas of the pavement surface bears the load from the tire and prevents the tire penetrating the spaces between the aggregates—thus reducing the contribution of the aggregate surface to the friction force by decreasing the tire-aggregate contact area (28).

4.3.3. Relationship between the Texture and Friction

The GN and DFT values both represent the friction properties of the pavement surface; however, the MPD values obtained by the LLS and CTM reflect the texture characteristics of the surface. To explore the relationship between the friction and texture, those two groups were plotted against each other in four different forms: GN vs. CTM, GN vs. LLS, DFT vs. CTM, and DFT vs. LLS.

Using statistical analysis, the correlation coefficient (R) was used to evaluate the relationships. The R ranges from -1 to +1, where negative and positive signs represent the negative or positive linear correlation respectively.

The statistical analysis shows that the relationship between the GN values and MPDs is strongly linear with high correlation coefficients (Figure 4.7). For the Grip-Tester performed at 50 km/h, the R = 0.83 was found for GN-CTM, and R = 0.82 for GN-LLS. In addition, higher correlation coefficients were observed at the speed of 70 km/h. The R values of 0.88 and 0.89 show a strong linear relationship between GN as a friction parameter, and MPDs of CTM and LLS, respectively.

From the results provided in Figure 4.7, the Grip-Tester data have a better relationship with texture compared to the DFT data in terms of the calculated R^2 values. Thus, it can be suggested that friction and skid resistance could be estimated by means of texture measurement data with high confidence.

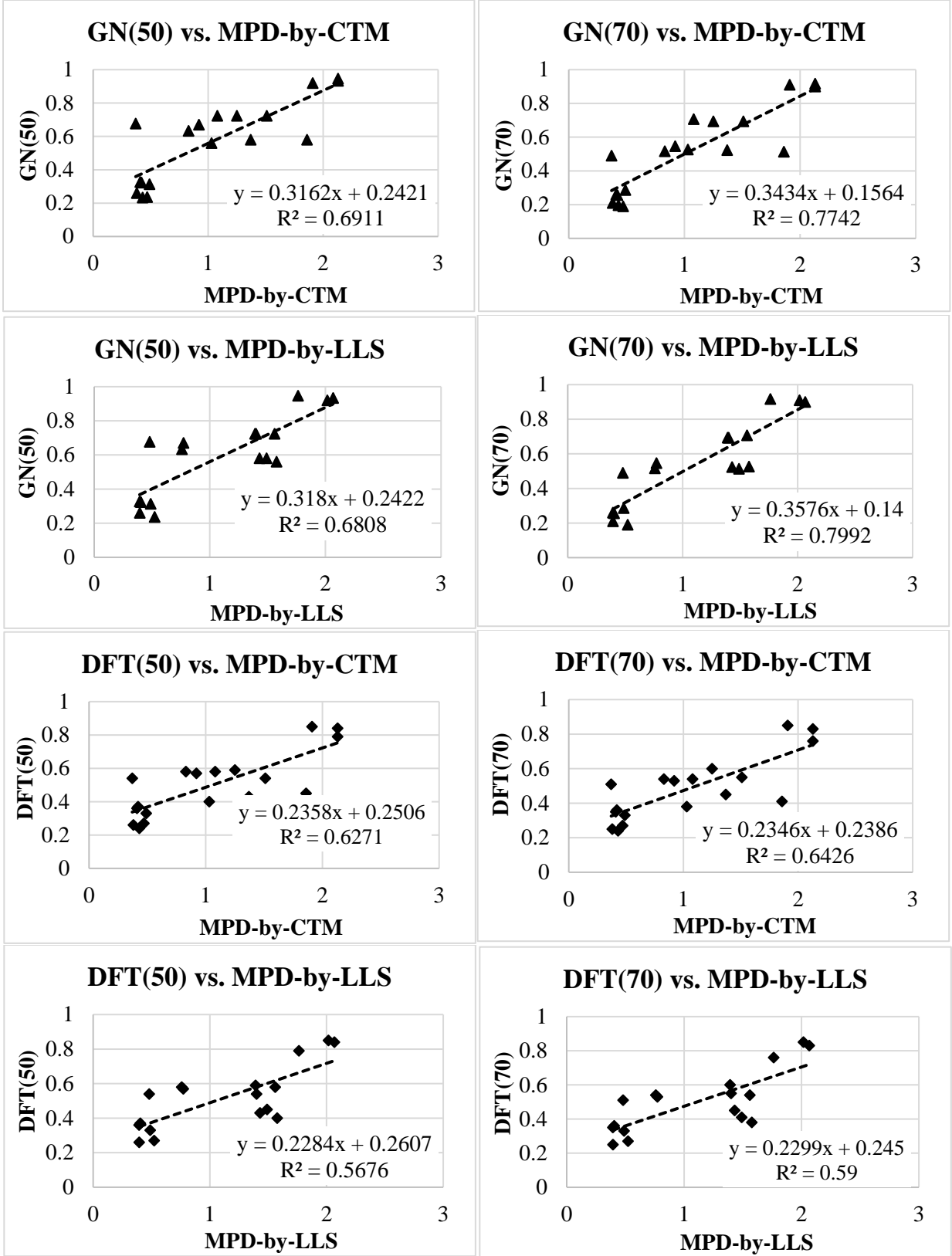


Figure 4.7 Plotted texture-friction data points including GN, DFT values, and MPD values

Chapter 5. Summary and Conclusions

In order to study the pavement and aggregate texture, a profile scanner prototype was developed that can capture both micro- and macro-texture. This prototype consists of a line laser scanner (LLS) mounted on a linear translation stage that can travel over a target and scan its surface. Several experiments such as error and tilt correction, developing a LabVIEW program, repeatability test, etc., were conducted by the research team to improve the developed LLS prototype's functionality. This prototype was used to study the texture of aggregates and pavement to find the relationship between texture and friction. From this research project, the following conclusions have been extracted and are presented in two parts addressing the various technical objectives set for this study.

5.1. Part 1: Aggregate Texture Measurement

The main scope of this part was to investigate the variation of wavelength ranges of aggregates surface to find those that affect their aggregate texture characteristics. The developed LLS prototype was used to capture the texture data of aggregates, and numerical methods were utilized to analyze the captured data. Some key findings of this study are summarized as follows.

- To study the effect of orientation, an aggregate was scanned in different orientations of 0° , 90° , 180° , and 270° . Comparison of PSD plots of data obtained at different orientations showed that the effect of aggregate orientation at the time of scanning is negligible.
- The PSD values of aggregates obtained from the same source were found to behave similar in the first decade of micro-texture. It can be concluded that the aggregate PSD values in the first decade of micro-texture significantly depend on their mineralogical properties.
- Based on the analysis conducted using the paired t-test, the PSD values of two aggregate types vary in the first decade of micro-texture. However, the PSD values could not be differentiated within the first decade of macro-texture since the PSD lines were nested in that range.
- The spatial signals were processed by means of band-pass filters to separate the micro-texture components. The texture parameters of R_q and R_p calculated in different filtered profiles were consistent with the PSD values within the wavelength range of 0.05 to 0.25 mm. It could be concluded that the wavelengths within the range make the greatest contribution to the texture friction.
- The results of PSD, R_p , and R_q were consistent with the Surface Aggregate Classification provided by TxDOT in which the aggregate A exhibited higher frictional properties compared to the aggregate B.

- The developed LLS is capable of differentiating aggregates at the micro-texture levels, and it is recommended that micro-texture should be included into the SAC classification to address the potential of the aggregate to provide surface friction.

5.2. Part 2: Correlation between Pavement Texture and Friction

This study investigated the relationship between the texture and friction of pavement surfaces using field-measured data. During this study, the LLS was used to measure the texture data along with the CTM. The MPD was adopted as a pavement texture indicator. DFT and Grip-Tester were employed for friction measurement. The efficiency and repeatability of the developed LLS were explored through comparison to the CTM results.

- The results of the repeatability analysis and standard deviation showed the reliability of the developed LLS prototype for pavement texture measurement. In all the test sections, the MPD calculated from the LLS data was similar to that calculated from the CTM data. Therefore, it is recommended that the developed LLS prototype should be considered as an efficient alternative to the CTM device, especially when three-dimensional texture data are needed.
- Regardless of the test speed and pavement type, the friction number obtained by the Grip-Tester showed a strong linear correlation with DFT measurements. Due to the reliable results of the Grip-Tester, its wider range of friction measurement, and the lack of need to control traffic, this device is recommended for use by state DOTs for friction measurement.
- The quality of the friction data obtained by a Grip-Tester seemed to be somewhat sensitive to the test speed, because the GN decreased slightly when the test speed increased from 50 km/h to 70 km/h (31 to 44 mph). This finding implies that keeping the test speed fixed at different test sections is important to achieving comparable results.
- The findings of the statistical analysis pointed to a strong positive linear correlation between texture and friction in pavements. The highest linear correlation coefficients (R) were observed between the GNs obtained at 70km/h (44 mph) and texture data obtained using either the LLS or the CTM.

References

- Abbas, A., M.E. Kutay, H. Azari, and R. Rasmussen. Three-Dimensional Surface Texture Characterization of Portland Cement Concrete Pavements. *Journal of Computer-Aided Civil and Infrastructure Engineering*, Vol. 22, 2007, pp: 197–209.
- Ahammed, M.A., and S.L., Tighe. Pavement Surface Mixture, Texture and Skid Resistance: A Factorial Analysis. Conference of Airfield and Highway Pavements, ASCE, 2008.
- Alazartech, Variable Frequency ADC Clock. <http://www.alazartech.com/Technology/Variable-Frequency-ADC-Clock>, Accessed January 1, 2017.
- Andriejauskas, T., V. Vorobjovas, and V. Mielonas. Evaluation of skid resistance characteristics and measurement methods”, 9th International Conference of Environmental Engineering, Vilnius, Lithuania, 2014.
- Araujo, V.M.C., I.S. Bessa, and V.T.F.C. Branco. Measuring skid resistance of hot mix asphalt using the aggregate image measurement system (AIMS). *Journal of Construction and Building Materials*, Vol. 98, 2015, 476–481.
- Asi, I.M. Evaluating skid resistance of different asphalt concrete mixes. *Journal of Building and Environment*. Vol. 42, 2007, pp. 325–329.
- Austrroads, 2005: Guide to the Management of Road Surface Skid Resistance. Sydney, Australia: Austrroads, 2005.
- Baraniuk, R. *Signals and Systems*. Rice University, Houston TX, 2009.
- Behrens, M.W. (1999), “Wet Weather Accident Reduction Program (WWARP)”, Highway Design Division Operations and Procedures Manual, Texas Department of Transportation, Austin, Texas.
- Cafiso, S. and S. Taormina. Texture analysis of aggregates for wearing courses in asphalt pavements. *International Journal of Pavement Engineering*, Vol. 8, 2007, pp. 45-54.
- Characterization of Pavement Texture by Use of Surface Profiles. ISO 13473-1, 1997, International Organization for Standardization.
- Characterization of Portland Cement Concrete Pavements. *Journal of Computer-Aided Civil and Infrastructure Engineering*, Vol. 22, 2007, pp: 197–209.
- Chen, B., X. Zhang, J. Yu, and Y. Wang. Impact of contact stress distribution on skid resistance of asphalt pavements. *Journal of Construction and Building Materials*, Vol. 133, 2017, pp.330–339.
- Descornet, G., B. Schmidt, M. Boulet, M. Gothie, M.T. Do, J. Fafie, M. Alonso, P. Roe, R. Forest, and H. Viner. HERMES Project: Harmonization of European Routine and research Measuring Equipment for Skid Resistance. FEHRL report, 2006.
- Do, M.T., and P. Roe, Report on state-of-the-art of test methods. TYROSAFE project deliverable D04, 2008.

- Gunaratne, M., N. Bandara, J. Medzorian, M. Chawla, and P. Ulrich. Correlation of Tire Wear and Friction to Texture of Concrete Pavements. *Journal of Materials in Civil Engineering*, Vol. 12, 2000, pp. 46-54.
- Hall, J.W., K.L. Smith, L. Titus-Glover, L.D. Evans, J.C. Wambold, and T.J. Yager. *NCHRP Project 01-43: Guide for Pavement Friction*. Transportation Research Board, Washington, D. C., 2009.
- Henry, J.J. NCHRP Synthesis of Highway Practice 291: Evaluation of Pavement Friction Characteristics. Transportation Research Board, National Research Council, 2000.
- Hoerner, T.E., and K. D. Smith. High performance concrete pavement: Pavement texturing and tire-pavement noise. Publication FHWA-DTFH61-01-P-00290. FHWA, U.S. Department of Transportation, 2002.
- Hsu, H.P. *Schaum's Outlines of Theory and Problems of Signals and Systems*. McGraw-Hill Companies, USA, 1995.
- Hu, L., D. Yun, Z. Liu, S. Du, Z. Zhang, and Y. Bao. Effect of three-dimensional macrotexture characteristics on dynamic frictional coefficient of asphalt pavement surface. *Journal of Construction and Building Materials*, Vol. 126, 2016, pp. 720–729.
- Huang, H. and J. Pan. Speech pitch determination based on Hilbert–Huang transform. *Journal of Signal Processing*, Vol. 86, 2006, pp. 792–803.
- Huang, Y. H. *Pavement Analysis and Design*. 2nd Edition. New Jersey: Pearson/Prentice Hall, 2003.
- Kane, M., I. Artamendi, and T. Scarpas. Long-term skid resistance of asphalt surfacings: correlation between Wehner– Schulze friction values and the mineralogical composition of the aggregates. *Wear*, Vol. 303, 2013, pp. 235–243.
- Karrenberg, U. *Signals, Processes, and Systems*. Third edition, Springer Heidelberg Dordrecht London New York, 2013.
- Kogbara, B.R., E.A. Masad, E. Kassem, A.T. Scarpas, and K. Anupam. A state-of-the-art review of parameters influencing measurement and modeling of skid resistance of asphalt pavements. *Journal of Construction and Building Materials*, Vol. 114, 2016, pp. 602–617.
- Laurent, J., Fox-Ivey, R., Dominiquez, F.S., and Garcia, J.A.R. (2014), ‘Use of 3D Scanning Technology for Automated Inspection Tunnels,’ Proceeding of the World Tunnel Congress 2014, Foz Do Iguaçu, Brazil.
- Mari, J.L, F. Glangeaud, and F. Coppens. *Signal Processing for Geologists and Geophysicists*. Editions OPHRYS, 1999.
- Masad, E., A. Rezaei, A. Chowdhury, and P. Harris. *Predicting Asphalt Mixture Skid Resistance Based on Aggregate Characteristics*. FHWA/TX-09/0-5627-1, Texas A&M University, 2009.
- Mataei, B., H. Zakeri, M. Zahedi, and F. M. Nejad. Pavement Friction and Skid Resistance Measurement Methods: A literature Review. *Journal of Civil Engineering*, Vol. 6, 2016, pp.537-565.

- MathWorks Inc. *Matlab-Getting Started Guide*. Natick, MA, 2016.
- Olshausen, B.A. *Aliasing, – Sensory Processes*. PSC 129, October 10, 2000, <http://redwood.berkeley.edu/bruno/npb261/aliasing.pdf>, Accessed January 1, 2017.
- Oppenheim, A., A.S. Willsky, and S.H. Nawab. *Signals & Systems*. Second edition, Pearson Education, 1998.
- Oppenheim, A.V., R. W. Schaffer, and J.R. Buck. *Discrete-Time Signal Processing*. Third Edition, Prentice-Hall Signal Processing Series, Pearson Education, 2009.
- Orfanidis, S.J. *Introduction to Signal Processing*. US ed Edition, Prentice Hall, 1995.
- Osgood, B. *Lecture Notes for the Fourier Transform and its applications*. Electrical Engineering Department Stanford University, 2007. <https://see.stanford.edu/materials/lsoftae261/book-fall-07.pdf>, Accessed January 1, 2017.
- Poon, C.Y., and B. Bhushan. Comparison of surface roughness measurements by stylus profiler, AFM and non-contact optical profiler. *Wear*, 1995, pp.76-88.
- Putman, J.A. *Signal Processing Techniques*. 2007. https://www.eeginfo.com/research/researchpapers/Signal_Processing.pdf, Accessed on Dec 21, 2016.
- Rado, Z. and M. Kane. An initial attempt to develop an empirical relation between texture and pavement friction using the HHT approach. *Wear*, Vol. 309, 2014, pp. 233–246.
- Roadway Departure Safety - Safety | Federal Highway Administration".Safety.fhwa.dot.gov. N.p., 2017. https://safety.fhwa.dot.gov/roadway_dept/, Accessed on February 20, 2017.
- Sandberg, U. Influence of Road Surface Texture on Traffic Characteristics Related to Environment, Economy, and Safety: A State-of-Art-Study Regarding Measures and measuring Methods. *VTI notat53A-1997*, 1998, Swedish National Road Association, Linköping, Sweden.
- Serigos, A.P., A.F. Smit, and J.A. Prozzi. Incorporating Surface Microtexture in the Prediction of Skid Resistance of Flexible Pavements. *Journal of the Transportation Research Board*, Washington, D.C., 2014, pp. 105–113.
- Sherrington, I., and E.H. Smith. Modern Measurement Techniques in Surface Metrology: Part II; Optical Instruments. *Wear*, 1988, pp.289-308.
- Slimane, A.B., M. Koudeir, J. Brochard, and M.T. Do. (2008), “Characterization of road microtexture by means of image analysis”, *Wear*, Vol. 264, 2008, pp. 464-468.
- Standard Practice for Calculating Pavement Macrottexture Mean Profile Depth*. ASTM E1845 – 2015, Philadelphia, Pennsylvania, American Society for Testing and Materials.
- Standard Terminology Relating to Vehicle-Pavement Systems*. ASTM E867 – 2012, Philadelphia, Pennsylvania, American Society for Testing and Materials.
- Stefan Torbruegge, S., and B. Wies. Characterization of pavement texture by means of height difference correlation and relation to wet skid resistance. *Journal of Traffic and Transportation Engineering*, Vol. 2, 2015, pp. 59-67.

- Texas Department of Transportation (TxDOT), (2016), “Bituminous Rated Source Quality Catalog (BRSQC)”, Construction Division, Materials & Pavements (CST-M&P).
<ftp://ftp.dot.state.tx.us/pub/txdot-info/cmd/mpl/brsqc.pdf>
- Thomas, L. Grip-Tester MK2 D-type Maintenance Manual. Issue 4, Findlay, Irvine Limited, Scotland, 2008.
- Thomas, L. Grip-Tester MK2 D-type Maintenance Manual. Issue 4, Findlay, Irvine Limited, Scotland, 2008.
- Vorburger, T.V., and J. Raja. *Surface Finish Metrology Tutorial*. NISTIR 89-4088, 1990.
- Wang, D., P. Liu, H. Wang, A. Ueckermann, and M. Oeser. Modeling and testing of road surface aggregate wearing behavior. *Journal of Construction and Building Materials*, Vol. 131, 2017, pp. 129–137.
- Wang, H., and Z. Wang. Evaluation of pavement surface friction subject to various pavement preservation treatments. *Journal of Construction and Building Materials*. Vol. 48, 2013, pp. 194–202.
- Wang, L., X. Wang, L. Mohammad, and C. Abadie. Unified Method to Quantify Aggregate Shape Angularity and Texture Using Fourier Analysis. *Journal of Materials in Civil Engineering*, Vol. 17 (5), 2005, pp. 498-504.
- Yoo, Y. Tutorial on Fourier Theory. 2001.
http://www.cs.otago.ac.nz/cosc453/student_tutorials/fourier_analysis.pdf, Accessed on January 18, 2017.
- Zhang, X., T. Liu, C. Liu, and Z. Chen. Research on skid resistance of asphalt pavement based on three-dimensional laser-scanning technology and pressure-sensitive film. *Journal of Construction and Building Materials*, Vol. 69, 2014, pp. 49–59.